ResearchGate

See discussions, stats, and author profiles for this publication at: https://www.researchgate.net/publication/8009156

Structural Analysis of Sterol Distributions in the Plasma Membrane of Living Cells

ARTICLE *in* BIOCHEMISTRY · APRIL 2005

Impact Factor: 3.02 · DOI: 10.1021/bi048172m · Source: PubMed

CITATIONS
34

READS
26

8 AUTHORS, INCLUDING:

Weimin Zhang
Samueli Institute
16 PUBLICATIONS **165** CITATIONS

SEE PROFILE

Todd Gruninger
Jesuit College Prep
15 PUBLICATIONS **149** CITATIONS

SEE PROFILE

Barbara Atshaves
Michigan State University
92 PUBLICATIONS **2,942** CITATIONS

SEE PROFILE

Jyh-Charn Liu
Texas A&M University
54 PUBLICATIONS **607** CITATIONS

SEE PROFILE

Available from: Barbara Atshaves
Retrieved on: 24 January 2016

Structural Analysis of Sterol Distributions in the Plasma Membrane of Living Cells

Weimin Zhang,[‡] Avery L. McIntosh,[§] Hai Xu,[‡] Di Wu,[‡] Todd Gruninger,[‡] Barbara Atshaves,[§] J. C. Steve Liu,*,[‡] and Friedhelm Schroeder[§]

Computer Science Department, Texas A&M University, College Station, Texas 77843-3112, and Department of Physiology and Pharmacology, Texas A&M University, TVMC, College Station, Texas 77843-4466

Received August 24, 2004; Revised Manuscript Received November 24, 2004

ABSTRACT: Although plasma membrane (PM) cholesterol-rich and -poor domains have been isolated by subcellular fractionation, the real-time arrangement of cholesterol in such domains in living cells is still unclear. Therefore, dehydroergosterol (DHE), a naturally occurring fluorescent sterol, was incorporated into cultured L-cell fibroblasts. Two PM markers, the enhanced cyan fluorescent protein (ECFP-Mem) and 3′-dioctadecyloxacarbocyanine perchlorate [$DiOC_{18}(3)$], were used to distinguish DHE localized at the PM of living cells. Spatial enrichment of DHE in the PM of living cells was visualized in real time by multiphoton laser scanning microscopy (MPLSM). Quantitative models and image-processing techniques were developed for statistical analysis of the distribution of DHE within the PM. The PM was resolved from the cytoplasm in a two-step process, and a smooth trajectory reference of the PM was refined by statistical regression and moments-based techniques. Thus, DHE intensities over the PM were measured following the major DHE intensity distributions. Spatial distributions of DHE within the PM were examined by a statistical inference technique, complete spatial randomness (CSR). For PM regions densely populated with DHE, the distributions of DHE exhibited statistical arrangements that were not *spatial random* (i.e., homogeneous Poisson process) or *regular* but, instead, exhibited strong *cluster* patterns. In effect, real-time MPLSM imaging data for the first time demonstrated that sterol enrichment occurred in clustered regions in the PM, consistent with the existence of cholesterol-rich domains in the plasma membrane of living cells.

Cholesterol is an essential component of cells and their membranes; it contributes to membrane permeability, fluidity, and activity of membrane enzymes or receptors and serves as a precursor to steroid hormones. Thus, cellular influx and efflux of this lipid must be tightly regulated to maintain a dynamic steady state and overall health of the cell. The mechanism(s) for transmembrane and intracellular cholesterol transport is (are) still emerging, and few techniques exist for real-time visualization of these pathways. Resolving the dynamics of cholesterol transport pathways and how cells maintain cholesterol homeostasis is critical to basic understanding not only of normal cholesterol homeostasis but also of abnormal cholesterol dynamics associated with atherosclerosis, cytotoxicity, Alzheimer's disease, diabetes, and obesity (reviewed in refs *1*−*5*).

Growing evidence suggests that plasma membrane cholesterol is organized into cholesterol-rich microdomains such as lipid rafts (e.g., caveolae) that are involved in multiple cellular functions including cholesterol transport, signaling, potocytosis, and the action of a variety of toxins (reviewed in refs *6*−*18*). Although the existence of cholesterol-rich and -poor regions in plasma membranes has been inferred from biochemical fractionation studies of cell plasma membranes (*19*−*24*) and from model membrane investigations (reviewed in refs *8* and *25*), it has yet to be demonstrated whether cholesterol is actually distributed into cholesterol-rich and -poor regions in the plasma membranes of living cells. It is not known whether such asymmetry is totally random or exhibits certain spatial "*patterns*" or "*signatures*" that can be generalized and used for correlation with physiological functions.

Major impediments to progress in this field have been (i) the absence of a selective, nonperturbing "tag" to detect cholesterol and (ii) the lack of noninvasive, nonperturbing techniques for real-time visualization of cholesterol structures in biological membranes of living cells. These obstacles have been overcome by the use of the naturally occurring fluorescent sterol dehydroergosterol (DHE)[1] and multiphoton laser scanning microscopy (MPLSM).

Dehydroergosterol (DHE) is an intrinsically fluorescent sterol found in high quantity in membranes of yeast and sponge (reviewed in refs *26* and *27*). DHE is readily taken up from the culture medium by microorganisms and cultured fibroblasts wherein it codistributes with endogenous sterol among intracellular membranes (replaces nearly 90% of endogenous membrane cholesterol) without altering cell

* To whom correspondence should be addressed. Phone: (979) 845-8739. Fax: (979) 847-8578. E-mail: jcliu@cs.tamu.edu.

[‡] Computer Science Department, Texas A&M University.

[§] Department of Physiology and Pharmacology, Texas A&M University, TVMC.

[1] Abbreviations: DHE, dehydroergosterol or Δ5,7,9(11),22-ergostatetraen-3β-ol; POPC, 1-palmitoyl-2-oleoylphosphatidylcholine; LUV, large unilamellar vesicles; ECFP, enhanced cyan fluorescent protein; DiO [$DiOC_{18}(3)$], 3′-dioctadecyloxacarbocyanine perchlorate; PM, plasma membrane; MPLSM, multiphoton laser scanning microscopy; CSR, complete spatial randomness; EDF, empirical distribution functions.

10.1021/bi048172m CCC: $30.25 © 2005 American Chemical Society
Published on Web 02/05/2005

growth, membrane fluidity, or sterol-sensitive enzymes and proteins in the plasma membrane (reviewed in refs *6* and *28*−*30*). Both the structural and functional properties of DHE closely mimic those of cholesterol in lipoproteins and membranes (reviewed in refs *6*, *23*, and *27*−*29*).

Although the above studies suggest that DHE would be an excellent probe molecule for detecting sterol and determining sterol distribution in the plasma membrane of living cells, unfortunately DHE absorbs in the ultraviolet (300−325 nm), and visualization of DHE by confocal and conventional fluorescence microscopy is complicated by significant photobleaching and toxicity (*31*, *32*). While ultrasensitive fluorescence video imaging circumvents some of these problems (*33*, *34*), video images are taken through the entire thickness of the cell and do not provide cross-sectional slices necessary for accurate determination of DHE distribution within the plasma membrane. However, advancement of recent fluorescence imaging technologies such as multiphoton laser scanning microscopy (MPLSM) and the use of nondescanned external detectors (*35*, *36*) has given researchers the ability to attain high-resolution images of multiple membrane and cellular forms of DHE in living cells (*23*, *31*). In contrast to confocal, conventional, and video imaging which require single photon ultraviolet excitation (in the range of 300−325 nm) of DHE (*31*, *33*), MPLSM utilizes infrared radiation and three-photon excitation to overcome these problems (*23*, *31*, *32*, *37*).

While MPLSM and DHE can provide high-resolution, real-time images of plasma membrane sterol in living cells, an equally important issue is the development of methodology for measuring and quantifying the new data. A consistent mathematical framework must be established for determination of DHE distributions within the plasma membrane. One of the noted works related to analysis of the image of plasma membrane is the spatial-temporal analysis approach (*38*), which is based on the image correlation spectroscopy technique (*39*). This approach is based on the theory that the time series of the relative intensity fluctuation of the signal are inversely proportional to the average number of independent fluorescent particles per laser beam area (*40*, *41*). The extension from time domain to spatial domain is particularly valid in a system with "monodisperse particles of uniform brightness" (*38*). In lieu of this transformation to the dynamic environment of the plasma membrane of living cells, new statistical approaches are necessary for the following reasons.

First, the thickness of the plasma membrane (<10 nm) (*42*) is much smaller than the MP excitation diameter of the laser beam (∼266 nm), and thus the beam will sample any aggregated data of the PM and also intracellular/extracellular components within its proximity. It is unclear whether one can directly apply the image correlation spectroscopy techniques on the plasma membranes of living cells, where organic metabolic processes are quite dynamic. (This system may not contain monodisperse particles of uniform brightness.)

Second, a central theme of this study is to examine the very nature of the cholesterol storage and transport under physiological conditions. It is necessary to employ a hypothesis-based testing approach to determine the spatial relationship of the observed cholesterol intensity distributions within the plasma membrane of living cells under physiological conditions where transport and metabolic processes are not slowed by lowered temperatures (*43*) and with image acquisition times of <10 s. New techniques are meant to utilize typical data acquisition methods with subsequent calculations to be performed on desktop computers.

The present investigation reports image-processing algorithms combined with statistical analysis methods to determine the statistical spatial properties of these distributions of dehydroergosterol (DHE). Cross-checking techniques that test hypotheses without using a (statistically) biased analysis methodology are developed for (a) imaging of living cells using multiple probes that discriminate PM from the intracellular region (cytosol) and (b) image segmentation techniques based on different algorithms. In the present analysis, the data show for the first time that sterol arrangement in plasma membranes of living cells was not random but clustered within specific interaction distances, consistent with nonuniform distribution of cholesterol in plasma membranes of living cells.

MATERIALS AND METHODS

Materials

The dehydroergosterol [Δ5,7,9(11),22-ergostatetraen-3β-ol] was synthesized as described elsewhere (*44*). 1-Palmitoyl-2-oleoylphosphatidylcholine (POPC) was obtained from Avanti (Alabaster, AL). Plasmid pECFP-Mem was obtained from Clontech (Palo Alto, CA). ECFP-Mem contains the N-terminal 20 amino acids derived from neuromodulin, which is posttranslationally palmitoylated and selectively targeted to the plasma membrane. The fluorescent probes Nile red and Vybrant DiO containing $DiOC_{18}(3)$ (3′-dioctadecyloxacarbocyanine perchlorate) were obtained from Molecular Probes (Eugene, OR). All glassware was sulfuric acid and/or solvent washed.

Methods: (A) Image Acquisition

Cell Culture and Overexpression of Enhanced Cyan Fluorescent Protein-Mem (ECFP-Mem). L-cells expressing ECFP in the plasma membrane were generated by stable transfection with 1 mg of the plasmid pECFP-Mem (Clontech) using Superfect (Qiagen, Valencia, CA) according to the manufacturer's instructions. Twenty-four hours after transfection, cell cultures were placed on selection medium containing G418 (700 mg/mL of medium). Resistant clones were selected and screened by PCR analysis and fluorescence imaging to ensure stable expression of pECFP-Mem.

Incorporation of Dehydroergosterol into Cultured Cells Overexpressing the Plasma Membrane Marker ECFP-Mem. To establish the distribution of fluorescent sterol at the plasma membrane of living cells using a plasma membrane protein marker, the fluorescent sterol dehydroergosterol (DHE) was incorporated into the cell plasma membranes of L-cells (L $arpt^-tk^-$) and L-cells overexpressing pECFP-Mem. Cells were cultured in Higuchi medium containing 10% fetal bovine serum and supplemented with 20 μg/mL DHE in the form of 10 mM 65:35 large unilamellar vesicles of POPC and DHE (*23*). The cells were cultured with the DHE for 2 days in two-well Lab-Tek chambered coverglasses (VWR, Sugarland, TX). Prior to imaging, the cells were washed with Puck's buffer.

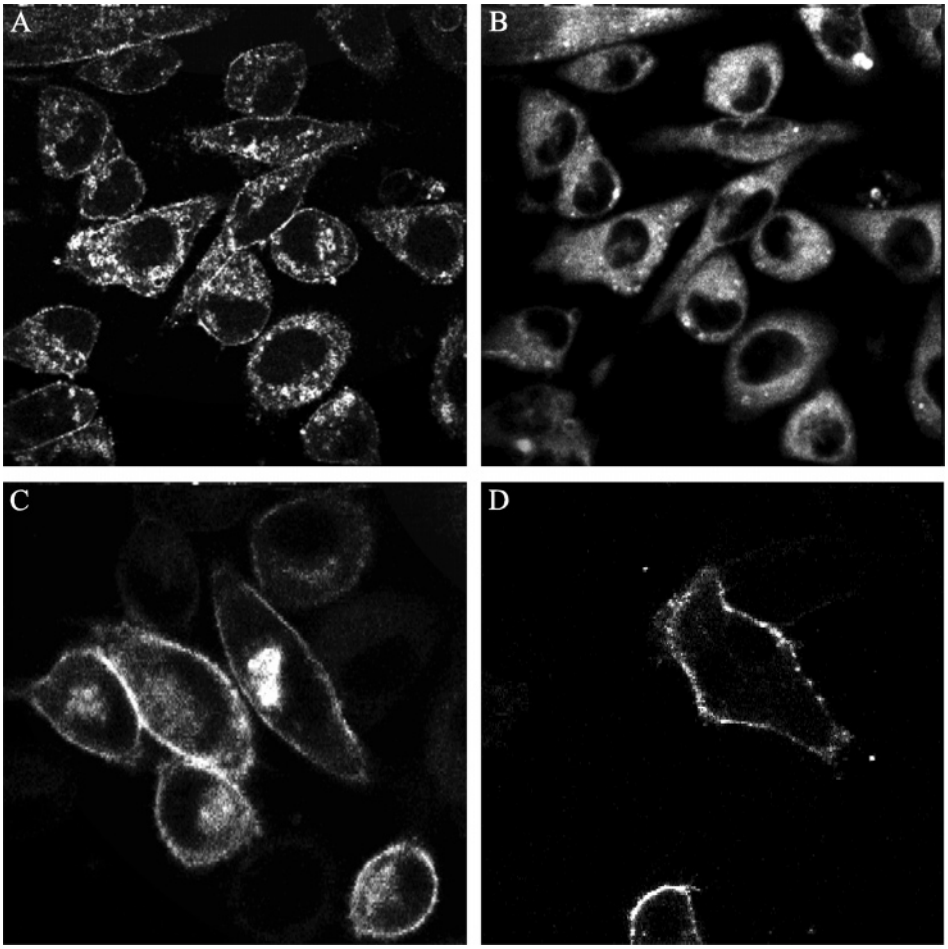

FIGURE 1: Multiphoton laser scanning microscopy (MPLSM) of living fibroblasts using 920 nm excitation. (A, B) L-cell fibroblasts were supplemented with dehydroergosterol in the form of LUVs and subsequently labeled with Nile red (as described in Materials and Methods). Dichroic filters were used to separate emission components in the wavelength regions from 360 to 430 nm (A, DHE) and from 525 to 650 nm (B, Nile red), respectively. (C) Plasma membrane demarcation was accomplished by transfecting the plasmid pECFP-Mem in L-cells. During MPLSM, fluorescence emission of the enhanced cyan fluorescent protein (ECFP) was detected in the wavelength region of 485−515 nm. (D) L-cell fibroblasts were labeled with $DiOC_{18}(3)$ and imaged by MPLSM with emission detection in the wavelength region of 485−515 nm.

Incorporation of Dehydroergosterol and the Lipidic Plasma Membrane Marker $DiOC_{18}(3)$ into Cultured Cells. The fluorescent sterol dehydroergosterol (DHE) was incorporated into the cell plasma membranes of L-cells (L $arpt^-tk^-$) or L-cells overexpressing ECFP-Mem as described in the preceding section. To determine the distribution of DHE in the plasma membranes of living cells, the plasma membranes were labeled with the plasma membrane probe Vybrant DiO [$DiOC_{18}(3)$], which was incorporated into L-cells (L $arpt^-tk^-$) according to the manufacturer's instructions as follows: cell media supplemented with DHE were removed and 100 μL of staining medium (5 μL of Vybrant DiO/mL of medium) was pipetted into a corner of the coverglass and gently agitated so that the cells were covered. The coverglass was incubated at 37 °C for 15−20 min and the medium drained off. This was followed by three wash cycles with fresh warm culture medium with incubation times of 10 min.

Incorporation of Dehydroergosterol and the Neutral Lipid Marker Nile Red into Cultured Cells. The fluorescent sterol dehydroergosterol (DHE) was incorporated into the cell plasma membranes as described in the preceding section. Nile red brightly stains neutral lipid droplets and intracellular structures containing neutral lipids in L-cells (*23*). To determine the usefulness of Nile red in resolving the cell boundary (when using a probe that has bright emission within the plasma membranes) from intracellular lipid droplets and membranes of living cells, these cells were also labeled with Nile red. Nile red was incorporated into L-cells (L $arpt^-tk^-$) and L-cells overexpressing ECFP-Mem by incubating the cells with 100−400 nM Nile red (Molecular Probes, Eugene, OR) for approximately 30 min.

Multiphoton Laser Scanning Microscopy (MPLSM). Images were acquired with a Bio-Rad MRC1024 multiphoton laser scanning microscopy (MPLSM) system equipped with Bio-Rad external nondescanned three-channel detectors as used in Figure 1A or external three-channel detectors provided by Dr. Warren Zipfel (Cornell University, Ithaca, NY) (Figure 1B−D). The overall system included an Axiovert 135 (Zeiss Inc., New York, NY) microscope with a Zeiss 100× Fluar (1.3 NA) oil immersion objective and a femtosecond Coherent Mira 900 Ti:sapphire laser pumped at 12 W with a Coherent Sabre Ar ion laser (Coherent, Palo Alto, CA). The Coherent Mira 900F was tuned to an excitation wavelength of 920 nm for simultaneous three-photon excitation of dehydroergosterol and two-photon excitation of the plasma membrane probes [ECFP-Mem and $DiOC_{18}(3)$] and Nile red. To prevent photobleaching and saturation of the excitation focal volume, the probes under-

going two-photon absorption at this excitation wavelength, ECFP-Mem and $DiOC_{18}(3)$, were imaged initially at 50% attenuation of the average laser power used for three-photon excitation of DHE. Total acquisition time of the sequential images was <10 s. Filters D375/50, D455/30, and HQ575/150 purchased from Chroma Technology (Brattleboro, VT) or with the INDO filter set supplied by Dr. Warren Zipfel provided separation of the fluorescence emission from DHE and the plasma membrane fluorescent probes used. The filter regions of this filter set comprised the 360−430, 485−515, and 525−650 nm ranges. The gain and black levels of each photomultiplier tube were optimized to minimize detection of background cellular autofluorescence. To minimize the effect of overlapped plasma membrane from upper and lower cell surfaces, a planar slice was chosen at a depth near the half-height of living cells grown on a chambered coverglass for subsequent data collection. The images of live cells were collected at 512 × 512 pixels with pixel sizes of 188 nm × 188 nm.

Plasma Membrane MPLSM Imaging with Nile Red, ECFP-Mem, and $DiOC_{18}(3)$. The distribution of DHE at the plasma membrane was visualized in real time using three independent fluorescent probe approaches.

First, dehydroergosterol-supplemented cells were incubated with Nile red as described above. Monomeric DHE and crystalline DHE were detected through Bio-Rad external detectors using D375/50 and D455/35 nm dichroic filters, respectively. The monomeric DHE was pseudocolored green while the crystalline portion was colored blue. No crystalline DHE was observed in the plasma membrane sections of the cells, confirming earlier results (*23*). Thus, in all following experiments potential contributions of crystalline DHE were neglected. The cells were simultaneously labeled with the neutral lipid stain Nile red (*23*), which was monitored through a HQ575/150 nm filter and pseudocolored red. Nile red and DHE were most highly colocalized in lipid droplets, producing a bright yellow intensity (red plus green), and Nile red was basically nondetectable at the plasma membrane (at these concentrations). Besides these bright structures, the Nile red emission was diffused over the entire intracellular cytoplasm. DHE clearly labeled a topological region that formed a contour around this area of diffuse Nile red intensity, apparently the plasma membrane. This contouring effect in the imaging plane provided the basis for determining the edge of the cell and therefore the plasma membrane. This was a result of a contrasting effect created by one probe with a strong intensity versus a probe with no or extremely low intensity within the PM. Subsequent statistical refinement allowed discrimination of DHE at the plasma membrane from DHE associated with intracellular lipidic structures.

Second, DHE was fed cells overexpressing the fluorescent plasma membrane protein marker ECFP-Mem, followed by incubation with Nile red for segmentation of plasma membrane. Once again, Nile red emission was seen throughout the intracellular regions of the cell but not at the edges of the cell wherein the plasma membrane marker ECFP-Mem produced bright intense fluorescence emission. Clearly, the L-cell plasma membrane was highly targeted by this modification, although not exclusively. The individual probe images were collected in real time in living cells by MPLSM using external detectors obtained from Dr. Warren Zipfel (Cornell University, Ithaca, NY) with the INDO filter set. DHE, ECFP-Mem, and Nile red emission was collected over the regions 360−430, 485−515, and 525−650 nm, respectively.

Third, L-cells were incubated with DHE, followed by incorporation of $DiOC_{18}(3)$ to cells as described above. $DiOC_{18}(3)$, a lipophilic oxacarbocyanine dye readily incorporated into membranes, produced bright emission at the plasma membrane under two-photon excitation as reported previously (*45*). The INDO filter set described previously was used to individually collect the emission from DHE and $DiOC_{18}(3)$.

Methods: (B) Image Analysis

A geographical contour of the membrane-rich portion of the cell was obtained using the Nile red image as a boundary reference to determine the statistical properties of DHE distributions over the detected PM area. Images were analyzed using application routines written in Microsoft Visual C#.Net, Matlab (Version 6.1) and R. To generate a collocating reference map for the membrane-rich area of the living cells, the DHE distributions were segmented or extracted from the images acquired via the Bio-Rad MRC-1024MP laser scanning microscopy system.

Multiple analysis techniques were used to determine the most likely PM areas and to cross-examine the consistency between different probe results. An overview of the image processing routines was diagrammed in Figure 2. Here, two segmentation techniques, simple subtraction (T1) and rank-statistic (T2), were used to compare the consistency of their analysis outcomes. Knowing that both T1 and T2 worked effectively for PM extraction, T2 was used to analyze two probing techniques based on ECFP (T3) and DiOC (T4). Pixelization of the PM images made it difficult to create a direct measurement reference along the PM trajectory. Subsequently, a moments function based technique was used to smooth the PM trajectory (T5) for intensity measurement. Finally, the completely spatial randomness (CSR) test was used to assert the statistical properties of the DHE intensity distributions (T6). Details of routines T1−T6 are discussed next.

T1: Plasma Membrane Image Extraction by a Simple Subtraction. In the image produced by the multiphoton laser scanning microscopy (MPLSM) technique, Nile red primarily accumulated in intracellular components and not the PM, while DHE not only labeled some intracellular components but also produced significant emission at the cell boundary just beyond the diffuse staining of the Nile red. This diffusive staining was quite low but above the noise level within the plasma membrane region. By using this lack of specificity of Nile red for the plasma membrane, an intensity differentiation technique proved useful. Through this technique, where the intensity of the red channel was subtracted from the green channel, the pixels along the PM area were isolated or segmented from the original image. Differences less than zero were set to zero while positive differences remain unchanged. After this protocol was applied to the enhanced red channel (Nile red), the coarse PM region in the green channel was produced albeit with some noise.

The step mentioned above accurately extracted the PM area, but it did not directly differentiate the PM from low-level noise, most of which was randomly scattered. The noise

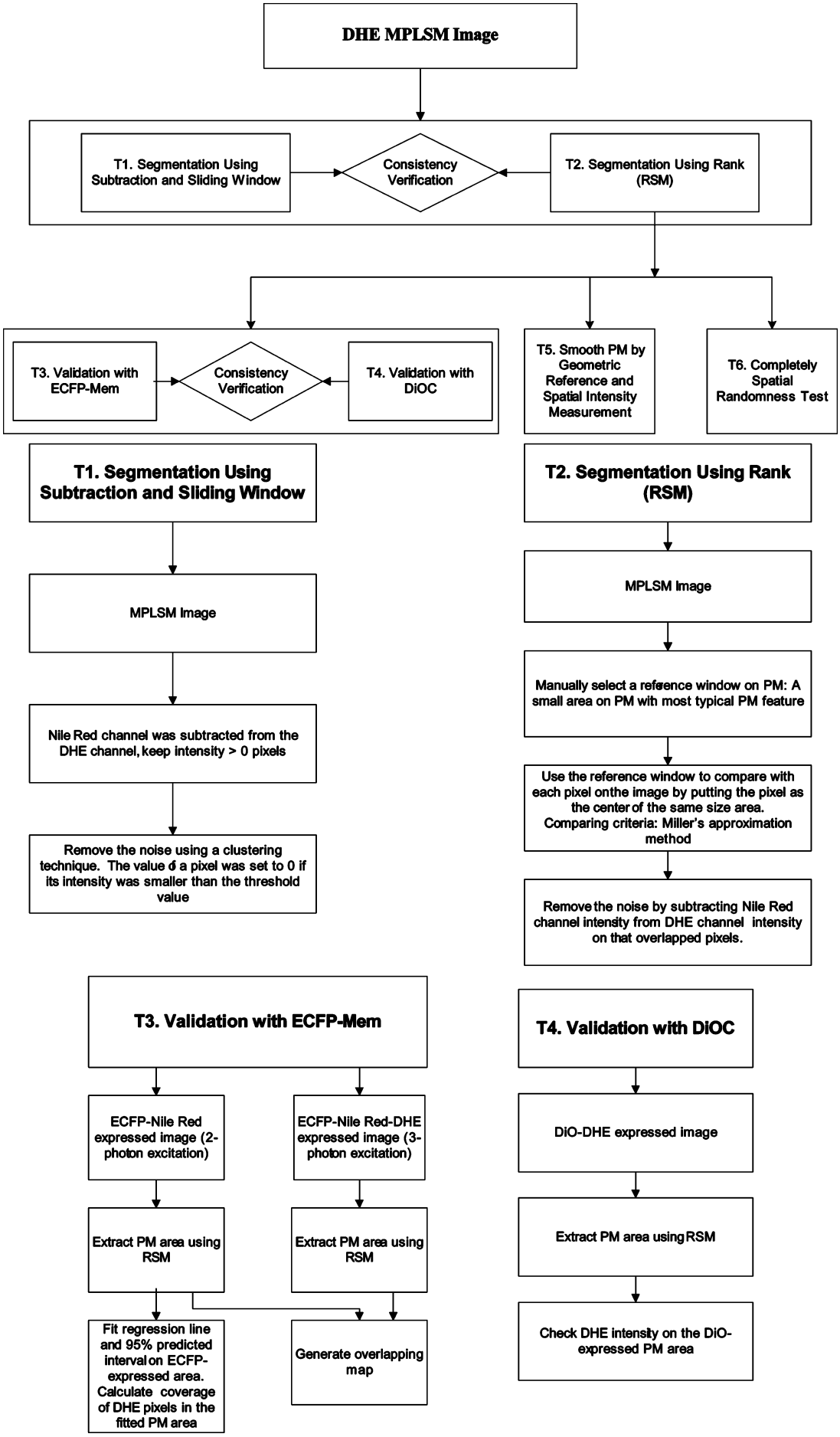
DHE MPLSM Image
T1. Segmentation Using Subtraction and Sliding Window
Consistency Verification
T2. Segmentation Using Rank (RSM)
T3. Validation with ECFP-Mem
Consistency Verification
T4. Validation with DiOC
T5. Smooth PM by Geometric Reference and Spatial Intensity Measurement
T6. Completely Spatial Randomness Test
T1. Segmentation Using Subtraction and Sliding Window
MPLSM Image
Nile Red channel was subtracted from the DHE channel, keep intensity > 0 pixels
Remove the noise using a clustering technique. The value of a pixel was set to 0 if its intensity was smaller than the threshold value
T2. Segmentation Using Rank (RSM)
MPLSM Image
Manually select a reference window on PM: A small area on PM with most typical PM feature
Use the reference window to compare with each pixel on the image by putting the pixel as the center of the same size area. Comparing criteria: Miller's approximation method
Remove the noise by subtracting Nile Red channel intensity from DHE channel intensity on that overlapped pixels.
T3. Validation with ECFP-Mem
ECFP-Nile Red expressed image (2-photon excitation)
ECFP-Nile Red-DHE expressed image (3-photon excitation)
Extract PM area using RSM
Extract PM area using RSM
Fit regression line and 95% predicted interval on ECFP-expressed area. Calculate coverage of DHE pixels in the fitted PM area
Generate overlapping map
T4. Validation with DiOC
DiO-DHE expressed image
Extract PM area using RSM
Check DHE intensity on the DiO-expressed PM area

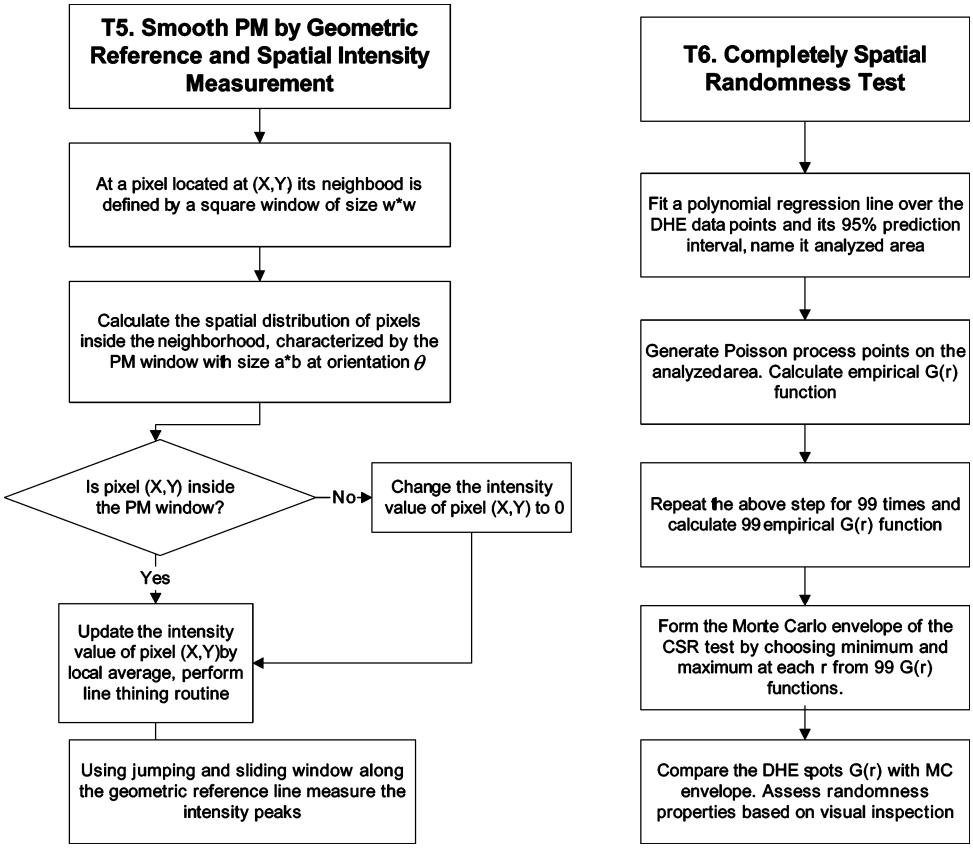

FIGURE 2: Flowcharts for image analysis. First, a schematic overview of the procedures involved in the image analysis: segmentation using subtraction (T1) and rank statistical method (T2), validation with ECFP-Mem (T3) and DiOC (T4), smoothing and geometric reference with spatial intensity measurement (T5), and completely spatial randomness test (T6). Second, flowcharts of the steps involved in each of these procedures, T1−T6, are shown in the following diagrams as discussed in Materials and Methods.

was removed by using a simple clustering technique and, in the process, advantageously derived a high-level classification of the PM regions based on their cluster sizes. An analysis *window* refers to a small number of adjacent pixels arranged in a particular shape (usually a square or rectangle), within which the pixels were analyzed using the image analysis algorithms. In the sliding window based analysis, two adjacent analysis windows overlap with each other while in the jumping window based analysis, no analysis windows overlap with each other. The sliding window based denoising technique was characterized by three parameters: window size, signal/noise ratio, and the intensity threshold values. In each analysis window, the ratio parameter measured the difference in densities between the signal and the noise. The value of a pixel was set to zero if its intensity was smaller than the threshold value.

T2: Plasma Membrane Image Extraction by a Rank-Statistic-Based Method (RCM). The PM region was also extracted using a *rank-statistic*-based technique (*46*). Essentially, this technique used a rank-based comparison rule to remove the intracellular and extracellular regions, with minimal elimination of the PM area. In the first step, a small window (with window size $k \times k$) was manually selected along the membrane, and then the whole image was searched with the same window size, pixel by pixel. By using a rank-based comparison procedure as shown in the Appendix 1, the intensity distribution in each window was compared with that of the seed window. The null hypothesis was that the color intensity distributions in two windows were identical. A separate test at each of three color channels was performed for acceptance or rejection of this null hypothesis. From this comparison procedure applied to the entire image, most of the cellular edge (PM) was segmented from the intracellular portion of the cell. A small number of dispersed intracellular pixels remained, but removal of the latter noise pixels was achieved for each experiment through a binary masking technique created by subtraction of the red and blue channel intensity from the green channel intensity. The mask's binary values of 0 and 1 represented the cases when the difference was negative or positive, respectively. This mask was then applied to the segmented data.

T3: Validating DHE Segmentation at the Plasma Membrane with ECFP-Mem as a Plasma Membrane Marker. To confirm the validation of our DHE PM segmentation technique, the experiment was repeated using Nile red again and a plasma membrane marker, ECFP-Mem, overexpressed in the cultured L-cells. The enhanced cyan fluorescent protein (ECFP) was excited through two-photon absorptive processes with relatively high quantum yield while monomeric DHE was excited through three-photon absorptive processes with a much lower quantum yield. The stronger laser excitation power needed for three-photon excitation of DHE produced significant bleaching effects of ECFP, so color images were obtained at different attenuation levels of excitation for this analysis. Furthermore, sensitivity levels were enhanced from the previous experiment as a result of different detector and filter sets. As a result, the image obtained at low excitation energy was used to define the ECFP-Mem, and the high excitation energy image was used to define the DHE labeling. Although ECFP-Mem was known to target the plasma

membrane of living cells, other intracellular membranes were labeled to a much lesser degree. The RCM was applied, utilizing the Nile red channel of both images (formed by low and high excitation intensity) in order to remove the intracellular labeled regions. It was determined that there was 60−80% overlapping of the DHE emission pixels with the pixels containing ECFP-Mem emission in the segmented regions.

Next, the hypothesis that the ECFP-Mem PM area followed a polynomial line was proposed. If this was valid, then based on our estimator of coefficients of this polynomial line, a 95% confident interval for our predicted membrane position could be given. This interval would cover DHE spots with 95% probability if DHE were also on the cell membrane region.

T4: Validating DHE Segmentation at the Plasma Membrane with $DiOC_{18}(3)$ as a Plasma Membrane Marker. To further validate the use of the above markers to help to segment the DHE localized at the plasma membrane, segmentation of the plasma membrane was repeated using a well-known lipophilic PM marker $DiOC_{18}(3)$. This cationic carbocyanine dye is known to have a higher level of partitioning into gel phases as opposed to fluid phases when the alkyl chains of the dye approximate the length of the lipid acyl chains combined with the lower headgroup. In the merged image, the red and green channels represented $DiOC_{18}(3)$ and DHE, respectively. This merged image was used to determine whether the segmented $DiOC_{18}(3)$ PM regions overlapped with DHE at the PM. The DHE channel was subtracted from the $DiOC_{18}(3)$ channel. When the difference was greater than zero, the mask value was set to 1; otherwise, it was set to zero. This binary mask was applied to the original data with the subsequent evaluation of the data revealing that there was 98% confidence overlap of the $DiOC_{18}(3)$ emission with the DHE emission at the plasma membrane segments.

T5: Establishment of a Geometric Reference and Spatial Measurement of DHE Intensity for Plasma Membrane Segmentation. The PM regions, even after being denoised, were highly irregular. Spatial measurement of DHE based on the raw data did not yield useful models because of the scattered local maxima/minima. To solve this problem, a smoothed geometric trajectory of the PM zone was obtained using moments functions (*47*), as shown in Appendix 2. After applying the steps to the entire image, the PM areas were transformed into smooth planar structures.

Next, each PM segment to be measured and analyzed for its DHE intensities was chosen, and a Matlab *line thinning* routine was used to reduce the segment into a single-pixel line. The thinning algorithm removed spurious edge points to a single reference line wherein the degree of connectivity can be preserved between discrete points. Empirically, 8-connectivity was used for the foreground objects, and 4-connectivity was used for background objects.

Selection of the PM segments for analysis turned out to be a nontrivial problem, because when the cell was imaged, the lamellipodia portions of adjacent cells tended to overlap more heavily with each other, making it less reliable for assessment of the DHE intensity distributions. As a result, only nonoverlapped PM regions were chosen, and five were randomly selected for analysis. DHE distributions were measured using both sliding window and jumping window techniques instead of measuring the DHE distributions pixel by pixel. More specifically, along the geometric reference line created by the aforementioned steps, the DHE intensities were determined within the specified *window size* and the *bin size*. The window size specified how wide the DHE measurement would be taken along the perpendicular directions of the current point on the reference line, and the bin size specified how far along the reference line to define a measurement window. All intensity values were summed in the window to represent the DHE intensity measurement.

Normality probability plots and the Anderson−Darling method were used on the DHE channel to check the normality assumption for intensity of this channel and found that it was not the case. On the basis of this observation *peak DHE spots* were defined as those pixels with intensities higher than the median intensity.

T6: Statistical Analysis of Spatial Distributions of DHE in the Plasma Membrane. The statistical properties of the spatial distributions of DHE spots were analyzed pixel by pixel. A two-dimensional spatial analysis was performed on the segmented data sets based on the complete spatial randomness (CSR) test and Monte Carlo simulation of the peak and of the full DHE spot data sets of the five PM segments, S1−S5, studied.

A spatial pattern was said to exhibit *complete spatial randomness* (CSR) if there was a high probability that it was a realization of a homogeneous Poisson process (*48*). If a pattern did not follow CSR, it was considered to be either *regular* or *clustered*, based on test outcomes. In a regular pattern, nearest neighbor distances between pixels would be larger than those from a CSR point pattern. In a clustered pattern, nearest neighbor distances would be less than those originating from a CSR point pattern. A major summary description of a statistical spatial pattern, $G(r)$ (*48*), measured whether the proportion of distance from an *event* to the nearest other *event* was at most r, where an event was any specific system state of interest, such as a pixel whose intensity was greater/smaller than a threshold value. The nearest neighbor distance,was defined in the present investigation as follows: for n spots in an area A of a PM segment, r_i denoted the distance from the ith spot to the nearest other spot in A. This typically included duplicate measurements between reciprocal nearest neighbor pairs. The *empirical distribution functions* (EDF), $\hat{G}_1(r)$, of the nearest neighbor distance were calculated by using the spatial Kaplan−Meier estimator of $G(r)$ (*49*) in this test.

Since the DHE spots were in a narrow area (PM), the distribution theory of these spatial point patterns was intractable. So, to test models against the data, the Monte Carlo test was used (*50*) as shown in Appendix 3. A total of 99 random samples of the same size as the pixels in our DHE sample under the hypothesis of CSR were simulated. DHE sample $\hat{G}_1(r)$ was compared with the Monte Carlo envelope formed by simulation data set to get the test result.

RESULTS

Intracellular Distribution of Probes Used To Distinguish DHE at the Plasma Membrane of L-Cell Fibroblasts. To visualize and determine the distribution of sterol in real time at the plasma membrane of living cells in culture, four different probe molecules were used. First, a naturally

occurring fluorescent sterol, dehydroergosterol (DHE), was incorporated into L-cell fibroblasts. While DHE could be added directly to the culture medium, the very low aqueous solubility of DHE resulted in formation of microcrystals adherent to the cell surface. Such microcrystals are endocytosed via the lysosomal pathway (*23*), but the presence of microcrystals (very brightly fluorescent) at the plasma membrane or within lysosomes readily saturated the photomultiplier and prevented detection of noncrystalline DHE throughout the rest of the PM. To avoid this potential interference, DHE was incorporated into large unilamellar membrane vesicles (LUV) comprised of POPC:DHE (65:35) as described in Materials and Methods. Three-photon-induced emission of DHE in the cells was imaged by MPLSM. Monomeric DHE (Figure 1A) was prominently visualized at the cell surface plasma membrane, in lipid droplets, and in intracellular membranes. There was almost no detectable crystalline DHE in the L-cells, confirming an earlier study (*23*). Second, L-cells were labeled with Nile red as described in Materials and Methods. The Nile red brightly stained neutral lipid droplets as well as other lipidic membranes (especially perinuclear) within the cell (Figure 1B) and a low intensity diffusive cytoplasmic labeling. However, Nile red was only weakly detectable at the plasma membrane (Figure 1B). Third, L-cells were transfected with pECFP-Mem to overexpress ECFP-Mem as described in Materials and Methods. Under two-photon excitation, ECFP-Mem exhibited bright staining of the plasma membrane and also some intracellular membranes as well (Figure 1C). Fourth, L-cells were labeled with $DiOC_{18}(3)$ as described in Materials and Methods. $DiOC_{18}(3)$ selectively stained the plasma membrane (Figure 1D).

In summary, the absence of crystalline DHE in the L-cells supplemented with POPC/DHE LUV allowed direct visualization of the monomeric DHE in the PM not only of monomeric DHE but also of the other probes used herein. Finally, the differential labeling of intracellular regions by Nile red and the plasma membrane by ECFP-Mem and $DiOC_{18}(3)$ suggested that DHE at the plasma membrane could be clearly distinguished from a majority of intracellularly localized DHE.

Colocalization of DHE with Neutral Lipid and Plasma Membrane Markers in Living L-Cell Fibroblasts by Multiphoton Laser Scanning Microscopy (MPLSM). As described in Materials and Methods, the naturally occurring fluorescent sterol, dehydroergosterol (DHE), was supplemented to control L-cell fibroblasts and L-cell fibroblasts overexpressing an enhanced cyan fluorescent protein that targets the plasma membrane (ECFP-Mem). Cells were then washed and incubated with Nile red (neutral lipid specific stain) or $DiOC_{18}(3)$ for colocalization. MPLSM with external detection was used to acquire the images of the probe combinations. Nile red (red pixels) brightly stained neutral lipid droplets within the cell while DHE (green pixels) labeled not only the plasma membrane but also neutral lipid-rich areas, e.g., lipid droplets (yellow/orange) within the L-cell interior (Figure 3A). To determine the distribution of ECFP-Mem versus Nile red, cells containing all three labels (ECFP-Mem, Nile red, DHE) were excited at low power (i.e., where DHE was not excited). Under these conditions, the ECFP-Mem was detectable at the plasma membrane (blue pixels) and in intracellular membranes but not lipid droplets (red pixels) within the cell interior (Figure 3B). To determine the distribution of ECFP-Mem versus DHE, cells containing all three labels (ECFP-Mem, Nile red, DHE) were excited at high power (i.e., where DHE was also excited). When the distribution of DHE (green) and ECFP-Mem (blue) was simultaneously visualized, the DHE and ECFP-Mem were both detectable at the plasma membrane (cyan pixels) (Figure 3C). To determine the distribution of $DiOC_{18}(3)$ versus DHE, cells containing both labels were simultaneously imaged, showing $DiOC_{18}(3)$ brightly staining the plasma membrane (red/orange) where DHE (green) was also detectable (Figure 3D). Thus, the use of multiple labels preferentially distinguishing intracellular organelles (Nile red) and the plasma membrane [ECFP-Mem and $DiOC_{18}(3)$] allowed distinction of the PM, DHE localized at the PM, and analysis of the DHE distribution in the PM of living cells.

Segmentation of the Plasma Membrane from MPLSM Images. Given that the physical structure of the PM in the images is made up of many optically resolvable morphological features that include microvilli, lamellipodia, filopodia, and large vesicles such as coated pits as well as membrane folds suggested the need for a comparison of different segmentation methods. These procedures would extract pixels containing the emission signal from fluorophores residing in the plasma membrane portion of the cell as opposed to the nucleus or cytoplasmic regions. The only topographical feature of the plasma membrane assumed a priori was that the PM formed a boundary around the intracellular portion of the cell. The objective was to produce a two-dimensional region with a 95% confidence interval containing the plasma membrane region no matter what the actual topography. Further refinement of this interval can be made and even a mean perimeter calculated by fitting a polynomial to this interval in order to perform subsequent analysis.

Thus, two different methods [simple subtraction method; rank-statistic-based method (RCM)] were used to extract the PM as described in Materials and Methods, and the comparative results are presented herein. The small white square (see arrow in third cell from the top left edge of Figure 3A) served as the seed for the searching process used in the latter RCM. The rank-statistic searching process (Figure 4A) with subsequent noise removal (Figure 4B) readily extracted the DHE in the plasma membrane of living L-cell fibroblasts imaged by MPLSM of Nile red/DHE (Figure 3A). The close correlation in DHE signal extracted for the PM as a result of the simple subtraction and sliding window denoising method versus the rank-statistic based with binary masking denoising method is shown in Figure 4C. In this figure, DHE detection areas were delineated with the following pseudocolors: pseudogreen represents the areas detected by both methods, pseudoblue represents the areas detected by the simple subtraction and denoising method only, and pseudored represents the areas detected by the RCM only.

While the simple subtraction and denoising method was effective in extracting the plasma membrane DHE (Figure 4C, green pixels), it did not completely eliminate all of the intracellular DHE (Figure 4C, blue pixels). In contrast, the RCM was based on a more quantitative treatment that was not only more efficient in extracting the DHE in the PM area (Figure 4C, green plus red pixels) but also more effective in removing intracellular DHE pixels (Figure 4C, no red pixels inside the cells). In using Nile red for extraction of

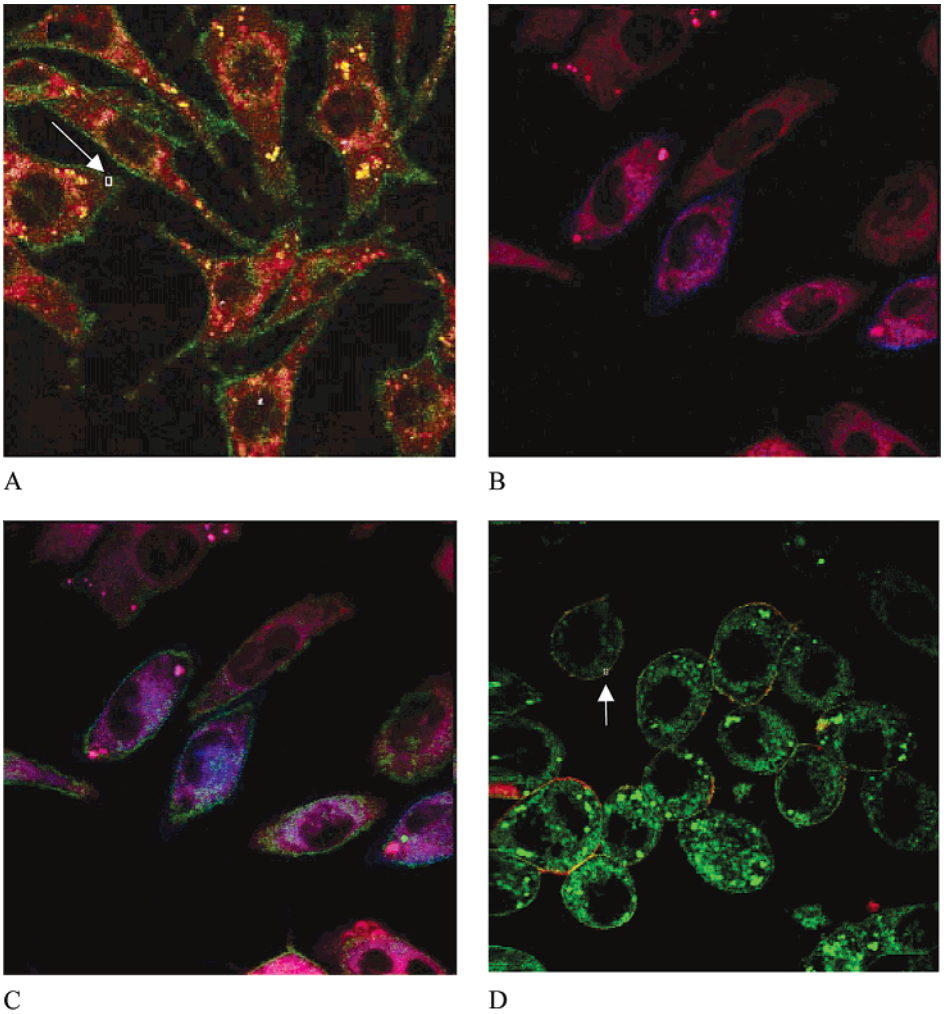

FIGURE 3: MPLSM of dehydroergosterol distributions in living fibroblasts using 920 nm excitation. (A) A merged image showing L-cell fibroblasts supplemented with DHE (green) in the form of LUVs and labeled with Nile red (red). The white square (see white arrow) represents the region chosen as a seed in the rank-statistic procedure. (B) A merged image of the plasma membrane marker ECFP-Mem (blue) expressed in L-cells with DHE (green) and also stained with Nile red (red); lower power for two-photon excitation. (C) A merged image with ECFP-Mem (blue) overexpressed in L-cells with DHE (green) and also stained with Nile red (red); higher power for three-photon excitation. (D) A merged image of L-cell fibroblasts labeled with the lipophilic probe $DiOC_{18}(3)$ (red) and DHE (green). Again, the white square (see white arrow) represents the region chosen as a seed in the rank-statistic procedure.

the plasma membrane, any structure or region containing Nile red would be subject to exclusion, which did not present any challenges for these techniques. However, any region close to the plasma membrane that does not have any fluorescence emission from Nile red but also contained emission from DHE would be subject to inclusion in the extracted PM. This effect was largely seen in the simple subtraction method as evidenced by the larger amount of intracellular DHE (Figure 4C, blue pixels). For its versatility, the RCM was adopted and used unless otherwise stated.

Segmentation by Nile Red in Comparison to a Fluorescent Protein PM Marker, ECFP-Mem. The RCM in combination with Nile red was used to extract the plasma membrane from cells overexpressing ECFP-Mem and labeled with DHE and Nile red as described in Materials and Methods. Due to the capacity of ECFP to be easily photobleached, two sequential images were taken at different powers of excitation. The low-power excitation image (Figure 3B) was used to define the distributions of ECFP-Mem within the plasma membrane since the lower intensity limited the amount of saturation and photobleaching. Due to three-photon processes, excitation of DHE was negligible under this initial power so that a higher power was necessary to obtain DHE emission (Figure 3C).

To examine the plasma membrane distributions, the extraction procedure was applied to both MPLSM images (Figure 3B,C), yielding the extracted results derived from low-intensity (Figure 5A) and high-intensity (Figure 5B) excitation powers. Only the Nile red (red) and ECFP-Mem (blue) channels were shown in Figure 5A while only the Nile red (red) and DHE (green) channels were shown in Figure 5B. A specific spatial region of the extracted plasma membrane was chosen and denoted S7 and S8 for the ECFP-Mem and DHE channels, respectively. Also, nonoverlapping pixels between the ECFP-Mem and DHE channels were removed, and the remaining 609 overlapped pixels were shown in black in Figure 5C. The amount of overlap between these two channels for the full plasma membrane area extracted for this cell was calculated to be 61.6% (Figure 5C). Furthermore, random selection of cells was made from 67 images collected as described in Materials and Methods. For each cell selected, the overlap rate ranged from 60% to 80% with the ECFP-Mem predicted interval always spatially encompassing the segmented DHE PM area.

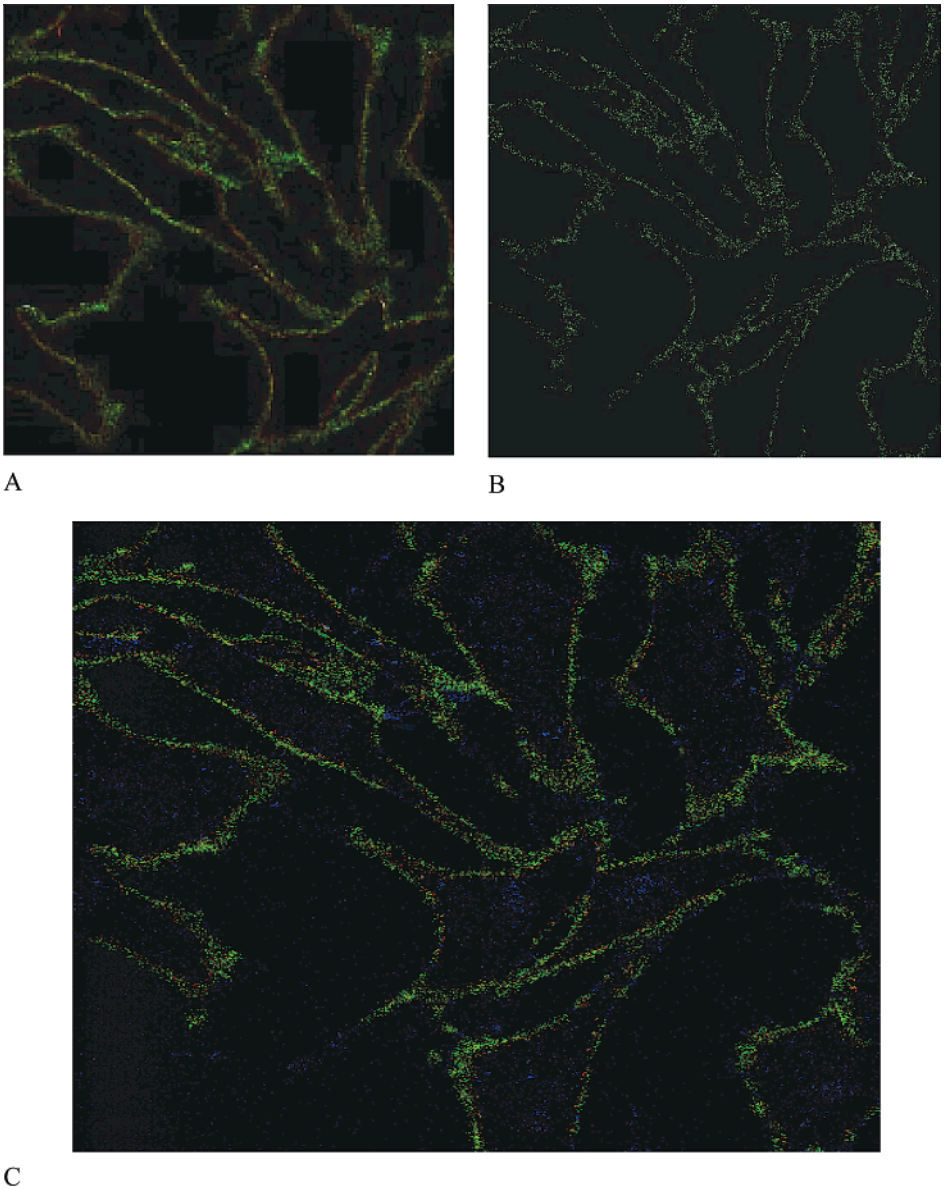

FIGURE 4: Plasma membrane extraction results and comparison from Figure 2A. (A) The comparison result of the PM extraction procedure using a rank-statistic segmentation procedure using a seed whose position and region are denoted by the white square in Figure 2A. (B) Result after removing noise from (A) through a binary masking technique. (C) Image of dehydroergosterol fluorescence detected at 350–400 nm and color-coded to illustrate the differences in the extracted PM areas by the rank-statistic method versus the simple subtraction method. Green pixels represent DHE emission segmented by both methods, blue pixels represent DHE emission segmented by the simple subtraction method only, and red pixels represent DHE emission segmented by the rank-statistic method only. The rank-statistic method with subsequent binary masking denoising technique provided the most effective segmentation result.

A 95% confidence level prediction interval was calculated for the ECFP-PM area in order to determine the overlap of segmented DHE. Two magenta lines forming the boundaries of this interval were overlaid upon the DHE distributions as shown in Figure 5B. Any pixels that fell outside this 95% confidence interval were counted in segments randomly chosen from different images. The average number of these DHE emission pixels outside the interval was determined to be 10.1% with standard deviance 2%. Thus, most of the segmented DHE overlapped with that cellular portion fluorescently outlined by the plasma membrane marker ECFP-Mem. Within the plasma membrane area represented by the 95% confidence interval, pixels of DHE represented about 45% of the plasma membrane. This suggested that larger concentrations of the fluorescent sterol, DHE, partitioned into a major part of the plasma membrane area.

Segmentation by the Lipophilic Plasma Membrane Marker, $DiOC_{18}(3)$. L-cell fibroblasts were supplemented with DHE in the form of LUVs for 2 days, washed, and labeled with $DiOC_{18}(3)$ as previously indicated in Materials and Methods. In this case, Nile red was not used since $DiOC_{18}(3)$ selectively stained the plasma membrane, and filter bleed-through would have complicated extraction procedures. A small section of the brightly stained region of the PM was chosen as the seed for the RCM procedure (small white square denoted by the white arrow in Figure 3D) with the extracted result presented in Figure 5D. The $DiOC_{18}(3)$ fluorophore (red pixels in Figure 5D) was highly localized in the PM area with almost no intracellular staining, so that the segmented DHE (green pixels in Figure 5D) was located solely on the plasma membrane. Varying levels of intensity occurred along the PM for both probes with some brightly

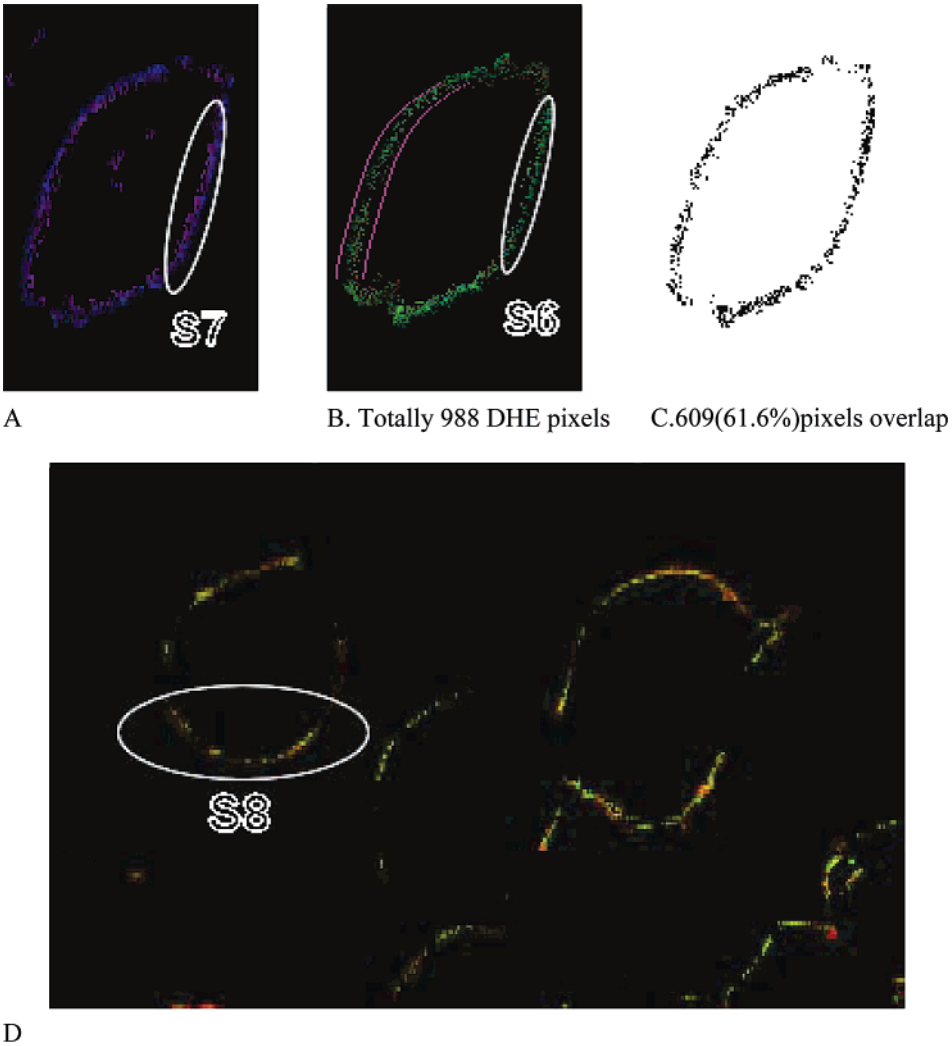

FIGURE 5: Plasma membrane segmentation results from Figure 2B,C (ECFP-Mem) and Figure 2D [$DiOC_{18}(3)$]. (A) The ECFP-Mem image segmentation result with S7 denoting the region of this image used for later statistical analysis. (B) Segmented PM area of DHE, superimposed with the predicted interval from PM-marker (ECFP-Mem) PM area. S6 marks the PM region chosen for later analysis. (C) Binary image formed from subtraction of (B) minus (A) to illustrate the localization of relative higher intensity DHE pixels colocalized with ECFP-Mem pixels in the plasma membrane segmented area. (D) $DiOC_{18}(3)$ and DHE segmented result from the white square in Figure 2D. $DiOC_{18}(3)$ was used for direct plasma membrane delineation. S8 marks the PM region chosen for later analysis.

overlapping pixels containing equivalent amounts of red and green intensity, as evidenced by the bright yellow pixels. Segment S8 (white oval in Figure 5D) was chosen for further statistical analysis from a cell without neighboring cellular overlap.

Smoothing Filtering Technique for Constructing a Reference Line along the Plasma Membrane. The objective of using a smoothing filtering technique on the PM was to create a geometric trajectory along the intensity centroid of the PM, so that the contour of the PM could be roughly followed. In principle, it was possible to directly trace and measure the DHE intensities over the extracted plasma membrane pixel by pixel. Unfortunately, this process was susceptible to discontinuous measurements, hence not accurately following the structure of the PM (data not shown). In contrast, a smoothing window filtering technique based on the moments function (Appendix, eqs 1−8) method was found to provide consistent results (Figure 6). Once the raw data were smoothed, a geometric reference line was synthesized for the PM, enabling smooth measurement and characterization of the patched DHE intensity distributions over the PM.

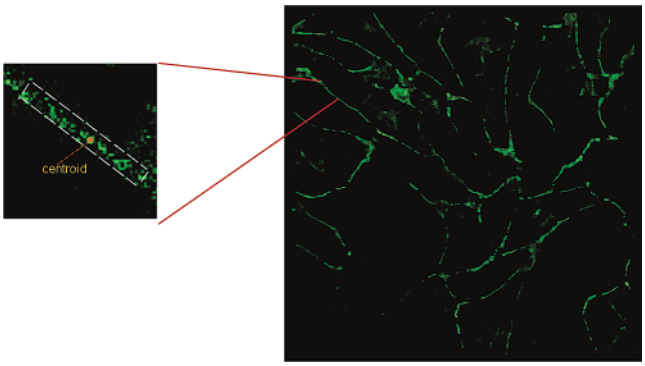

FIGURE 6: Image smoothing using a nonlinear median window filter based upon a moments function. The smoothed image shows the result after application of a continuous planar model of the DHE image using window size 20 × 20 and neighborhood 5 × 5. Each pixel in the smoothed image represents the intensity centroid calculated from the application of this filter to the raw data. A blowup of a particular plasma membrane region from the raw data was shown to illustrate the window and its intensity centroid.

The smoothing algorithm was essentially a nonlinear median filter, where the size of the PM window changed

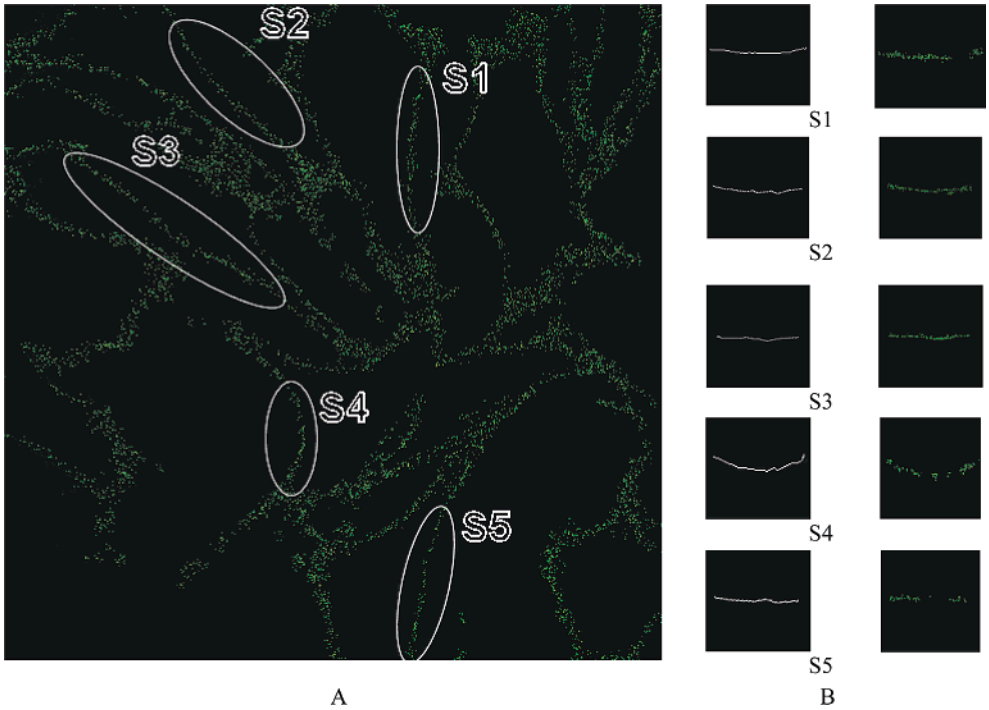

FIGURE 7: Five segments of the dehydroergosterol emission in rank-statistic extracted plasma membranes from MPLSM images of living fibroblasts. (A) The monomeric DHE along the plasma membrane with the five segments marked that were used for spatial measurement study. (B) The geometric reference lines from a Matlab thinning routine on the PM and the corresponding raw data values for each segment.

with the intensity distributions of the DHE within each smoothing window (zoomed raw data image in Figure 6). The size of the PM window of the intensity centroid for each smoothing window diminished with sparseness of the DHE pixels. As a result, a chance for the central pixel in the current smoothing window being retrained also diminished with implication that this procedure tended to eliminate isolated spots and preserved dense signals, regardless of their amplitudes. This was evidenced by the fact that both strong and weak DHE patches were captured in the resulting image. The shallow patches within the cell were not removed from the smoothing process, but their presence did not affect our study because only a few selected PM segments were used for spatial analysis.

Selection of Plasma Membrane Segments for Measurement and Analysis. Selection of the PM segments for statistical analysis was critical to the analytical modeling. PM segments from cells overlapping each other were avoided. The segments chosen consisted of two types: high DHE density or low DHE density. The set of DHE measurements was extracted from the DHE and Nile red image (Figure 3A) to produce the DHE measurement map (Figure 7A). On the basis of the experimental procedures and from visual inspection of the image, PM regions that exhibited fairly clean signals without overlapped readings were chosen. From these regions, five PM segments (S1−S5) were randomly selected and used in the subsequent spatial measurement and analysis.

Geometric reference lines were produced for the five segments using a Matlab thinning routine for determining the trajectory along each of the raw data segments (Figure 7B). These reference lines approximately represented the central points of the DHE intensity over the PM "band/belt." However, other types of alternative reference lines, such as using the interface between PM and cytosol, provided similar data.

To validate the use of Nile red in the segmentation procedure and to compare plasma membrane distributions of DHE with those of the plasma membrane protein marker, ECFP-Mem, segment S6 (Figure 5B) from the DHE channel and segment S7 (Figure 5A) from the ECFP-Mem channel were chosen using the criteria mentioned above.

Next, in using a lipophilic membrane marker, $DiOC_{18}(3)$, to segment the PM area, the merged segment S8 (Figure 5D) was picked for examination and comparison of the DHE distributions from this extraction procedure to those obtained utilizing Nile red. Also, the DHE distributions were compared to the carbocyanine dye distribution itself. This segment contained both the DHE channel (green) and the $DiOC_{18}(3)$ channel (red), which was subsequently separated for further analysis.

Intensity Measurements of DHE in the Plasma Membrane Segments. The physical measurements of S1−S5 (Figure 8) were obtained using jumping windows (column A) and sliding windows (column B), respectively. In each case, the intensity was well below the maximum value of the display dynamic range, indicating the carefully controlled experimental process to keep the imaged cells alive.

In the jumping window mode, local peaks had the potential of being missed when located between two adjacent windows. On the contrary, certain data in the dense DHE locations were counted twice in the sliding window mode. The number of peaks was determined for each of the segments S1−S5: 13 peaks for S1, 19 peaks for S2, 19 peaks for S3, 10 peaks for S4, and 9 peaks for S5. These peak numbers were hypothesized to be the number of DHE clusters along the membrane. Also, for the DHE traces generated from both techniques, the DHE intensity distribution was highly discrete and scattered. Normality testing as

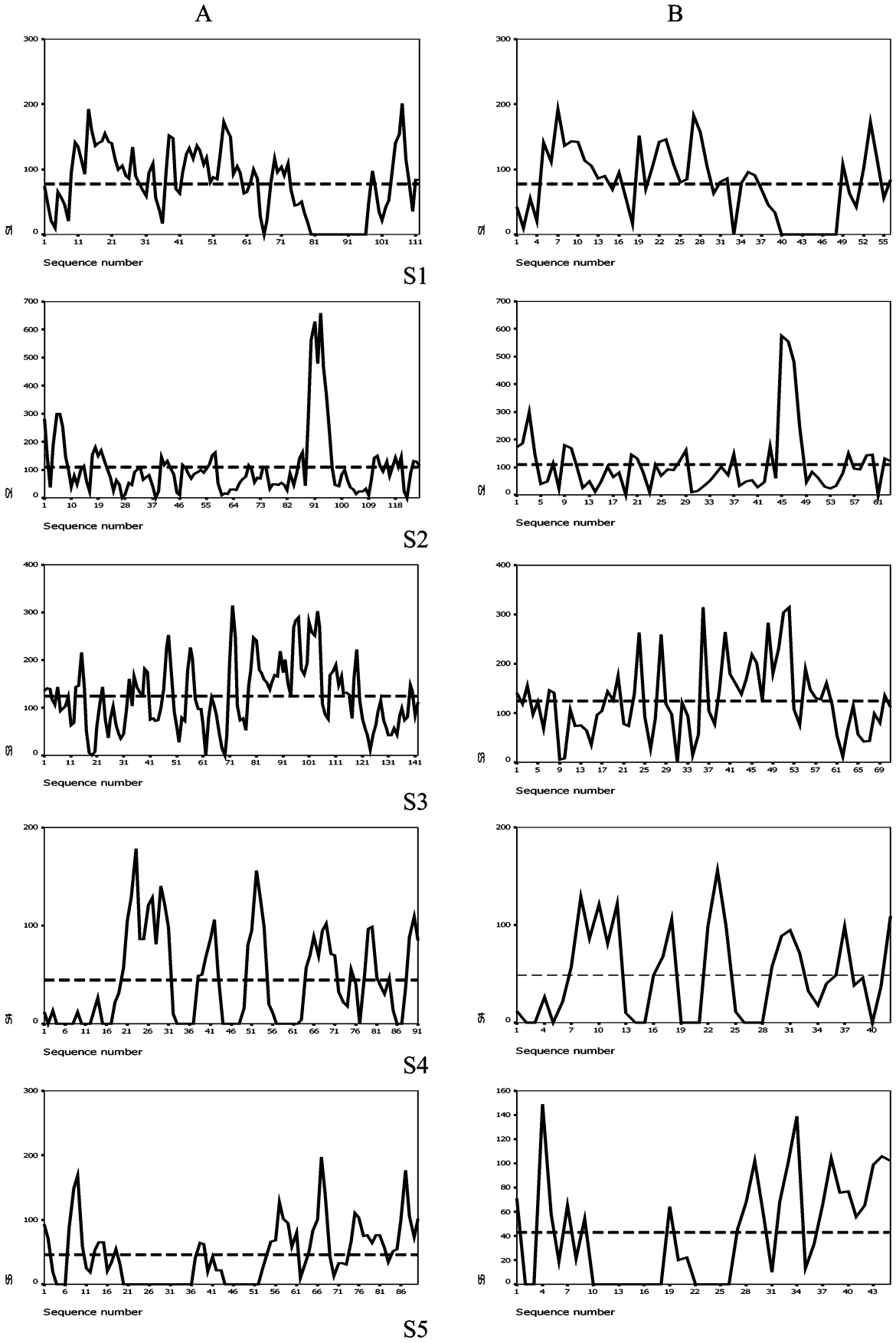

FIGURE 8: Intensity measurement of DHE along plasma membrane segments of different cells. DHE intensity measurements from segments 1−5 using a sliding window (A) and a jumping window (B), with window size 10 and bin size 3. The vertical axis represents the sum of the intensities within the window, while the horizontal axis represents the window sequence number. The dashed line represents the mean intensity over the segment sequences.

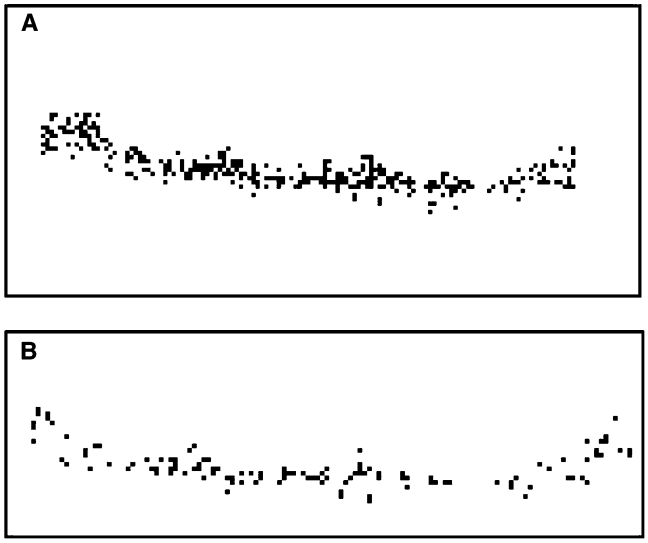

FIGURE 9: Zoomed images comparing thresholded (peak) data to the full data set of a typical plasma membrane segment of DHE emission detected over the wavelength region 350−400 nm. (A) Image before 50% thresholding was applied. (B) Image after 50% thresholding was applied.

applied to the intensity distribution indicated that the intensity spectrum did not conform to a normal distribution.

Furthermore, for S1−S5, the number of peak DHE pixels (using a 50% threshold) as well as the total number of pixels within a 95% confidence interval was defined as the plasma membrane. These values were then used to calculate the PM area enriched in DHE: (S1) 8.51%, (S2) 11.2%, (S3) 12.83%, (S4) 9.69%, and (S5) 8.31%. These data implied that 10.1 ± 0.9% of the PM was highly enriched in sterol. Likewise, using the full DHE data set, a value of 27 ± 4% was calculated for the percentage area of the PM that contained detectable amounts of DHE. This calculated percentage was highly dependent upon detection sensitivity.

Statistical Analysis of the Spatial Properties of DHE in the Plasma Membrane. Statistical analysis on the spatial properties of the DHE locations was performed using the *R* system (*51*) to implement analytical models (see Materials and Methods). This analysis was focused upon the spatial locations of DHE pixels whose intensities were above various threshold values. Typical PM segments before (Figure 9A) and after (Figure 9B) removal of DHE pixels with values below the median value were analyzed to generate a spatial map of the peak DHE pixels, whose intensities represent strong dehydroergosterol emission.

The objective of the complete spatial randomness (CSR) test was to examine the statistical spatial nature of the data set. The CSR test was applied to the eight data sets in the preceding section. In this approach, the proportion of nearest neighbor distance in the data set was compared to that of simulated homogeneous Poisson process data. The position of the peak DHE data points from S1 was plotted (Figure 10A). To isolate the PM area, a polynomial line was fitted using linear regression over these points, and a 95% prediction interval was calculated for this regression line. The two lines (Figure 10A) were drawn to illustrate the spatial localization of this predicted interval in addition to the location of the DHE pixels. Subsequently, 99 simulations were performed in this particular interval. For illustrative purposes, a simulation was presented in Figure 10B. At each nearest neighbor distance r, 99 $\hat{G}_1(r)$ were calculated utilizing Monte Carlo simulations. The Monte Carlo envelope, the maximum and minimum for $U(r)$ and $L(r)$, was taken from these 99 $\hat{G}_1(r)$. The upper and lower bound of this envelope was represented by dashed lines in Figure 10C and the estimated G function from our peak DHE data set S1 as a solid line. Since the smallest nearest neighbor distance between any two pixels was one, those distances below one pixel were neglected. Clearly, the data set has higher nearest neighbor distance proportion than that of the homogeneous Poisson process upper bounding envelope, showing an obvious cluster pattern. The same test result from the S1 full data set also gave a similar result (Figure 10D). Although results were shown only for CSR tests of peak and full DHE data sets of S_1, the same test procedures were applied to all the five segments, both for the peak DHE data set and for the full raw data sets. In the "nearest neighbor EDF" plots, all of the small $\hat{G}_1(r)$ values were larger than the upper bound of the Monte Carlo envelope, indicating that the peak and full DHE spots have markedly higher proportion in the small nearest neighbor distance than that of Poisson process. This result explicitly indicated that the DHE pixels exhibited a clustered pattern.

Comparison Study of DHE and ECFP-Mem Spatial Properties in the Plasma Membrane. The spatial properties of ECFP-Mem and DHE were examined by statistical analysis. Once again, a spatial plot of the position of peak DHE pixels was constructed (Figure 11A). Peak DHE pixels from segment 6 (S6; Figure 5B) were determined by using a threshold at the 85 percentile. Similarly, peak ECFP-Mem spots in segment 7 (S7; Figure 5A) were obtained using the same threshold and plotted (Figure 11B). Due to the greater detection of dehydroergosterol emission from increased filter transmission and bandwidth, this threshold was also increased for a closer comparison to the initial experiment (Figure 3A). With this enhanced sensitivity, emission from lower concentrations of DHE combined with low-level autofluorescence was detected. Since the primary focus was on regions of sterol enrichment, the threshold was increased to select the higher peak pixels while eliminating these "noisy pixels". The empirical G function was calculated from the peak DHE data set and its 99 simulation Monte Carlo envelope (Figure 11C). Similar calculations were performed for the peak ECFP-Mem data set (Figure 11D). In comparing the two G functions estimated result, both ECFP-Mem and the DHE had the statistical cluster property, although under the same threshold, the peak ECFP-Mem data set had a larger estimated probability over the same nearest neighbor distance than the peak DHE data set.

The correlation coefficients were calculated between DHE and ECFP-Mem. Two directional approaches were used since DHE was not always colocalized with ECFP-Mem: ECFP-Mem to DHE channel and DHE channel to ECFP-Mem. The calculated correlation coefficients were 0.1272 and 0.2992, respectively. The correlation was significant as the p-values for both calculations were <0.0001. Clearly, the intensity of DHE was positively correlated with that of ECFP-Mem.

Comparison Study of DHE and $DiOC_{18}(3)$ Spatial Properties in the Plasma Membrane. For direct visual comparison between the two probes, the positions of peak DHE spots and peak $DiOC_{18}(3)$ spots were plotted (Figure 12A,B), both using the 85 percentile threshold. These peak spots repre-

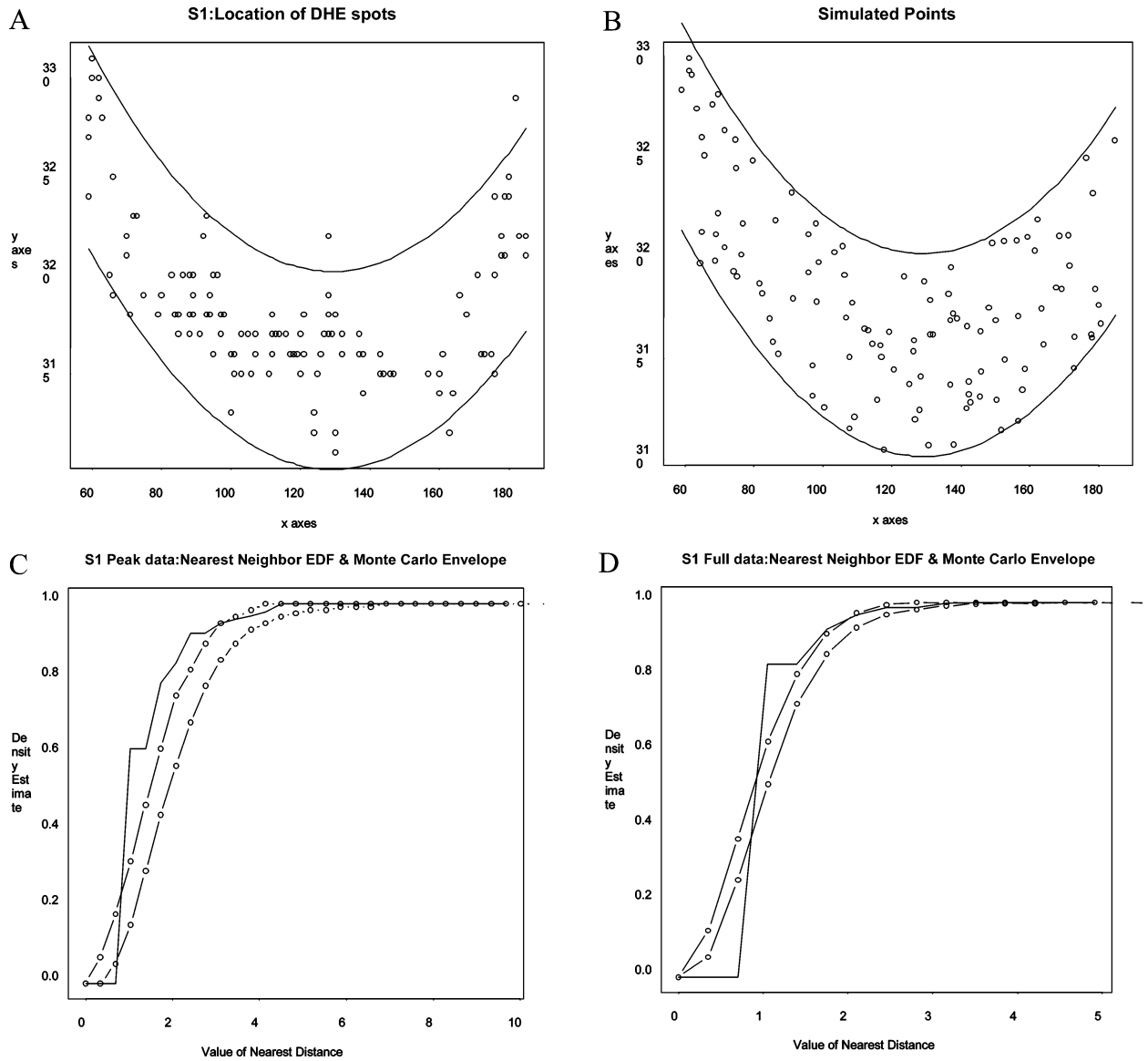

FIGURE 10: Statistical analysis results for S1. (A) A spatial plot of peak DHE pixels with curves marking the location of the 95% prediction interval. (B) Simulated CSR points in this same spatial interval. (C) The nearest neighbor EDF plot (line) and Monte Carlo envelope from 99 simulations for the peak DHE data set and (D) for the full DHE data set.

sented about 4% of the segmented PM area in comparison with the full data set, which represented 40% of the segmented PM area. The *G* function of DHE peak data and its Monte Carlo envelopes were shown in Figure 12C while the same result for the peak $DiOC_{18}(3)$ data was shown in Figure 12D. Both the DHE and $DiOC_{18}(3)$ have similar results with high estimated probability over their nearest neighbor distance with strong cluster property. In this comparison, the estimated probability was much higher than the results from the previous analysis.

The correlation coefficients were calculated between $DiOC_{18}(3)$ and DHE. Again, two approaches were used since not every DHE pixel was overlapped with a pixel containing $DiOC_{18}(3)$ emission: $DiOC_{18}(3)$ channel to DHE channel and DHE channel to $DiOC_{18}(3)$ channel in this image. The results were 0.4056 and 0.4469, respectively, for the two approaches with *p*-values <0.0001 for testing the hypothesis of no correlation. Each *p*-value was the probability of observing a correlation as large as the observed value by random chance, when the true correlation is zero. The positive correlation between the DHE channel intensity and $DiOC_{18}(3)$ channel intensity was quite significant as determined from the low *p*-value. This revealed that for a position along the plasma membrane area with high-intensity $DiOC_{18}$-(3) might also have high-intensity DHE.

DISCUSSION

As previously indicated, while cholesterol-rich and -poor domains have been detected by biochemical fractionation of the cell/plasma membrane (*19*, *20*, *22*−*24*) or model membranes (reviewed in refs *8* and *25*), it is not yet clear whether such cholesterol-rich and -poor domains exist in the plasma membrane of living cells.

The issue of demonstrating cholesterol enrichment in the plasma membrane was recently overcome by directly visualizing DHE in living cells with multiphoton laser scanning microscopy (MPLSM) (*23*, *31*, *32*). Clearly, bright dehydroergosterol emission occurred around the perimeter of the cell, but this region was not contiguous and the intensity

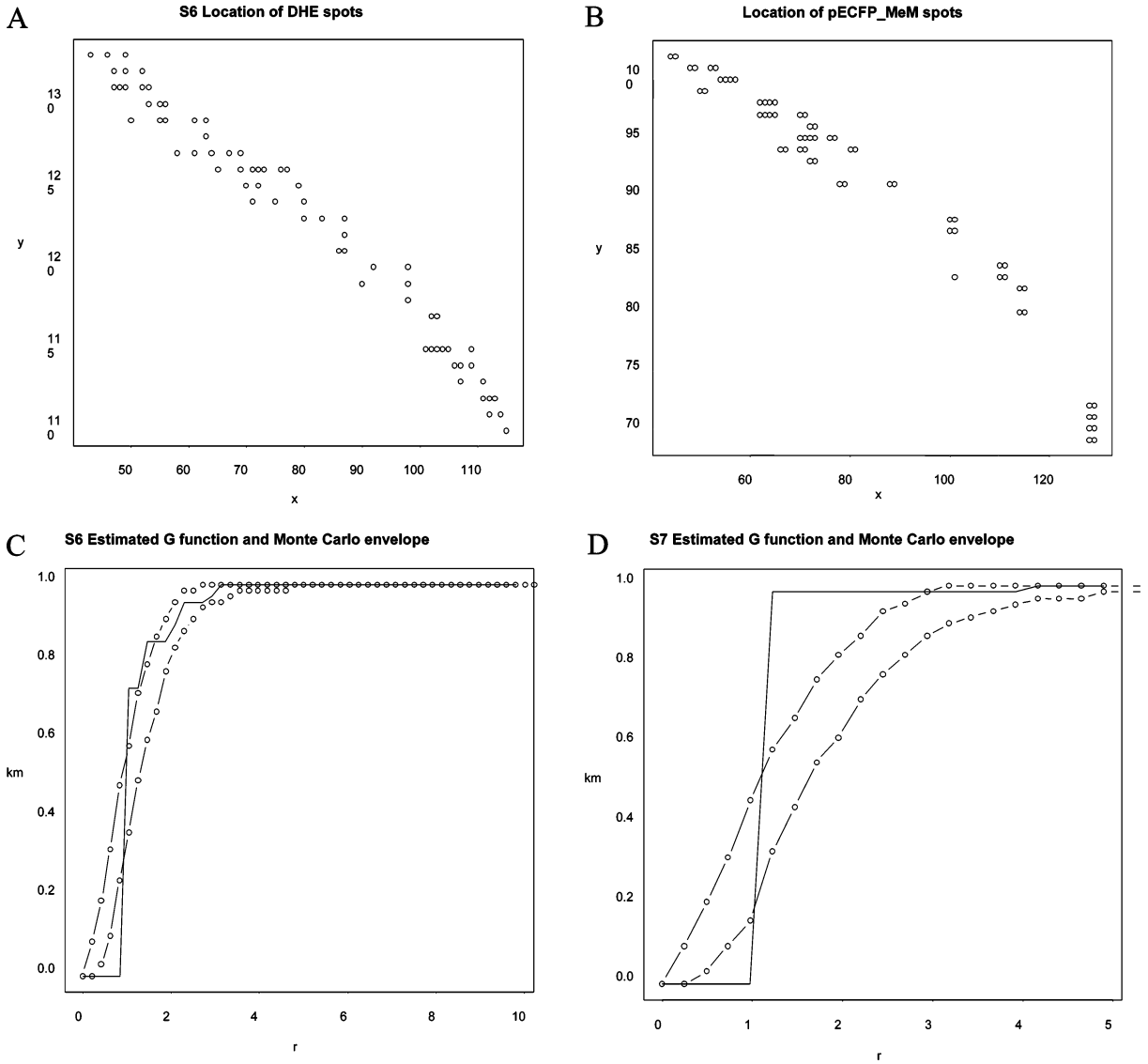

FIGURE 11: Statistical analysis results for S6/S7. (A) Location of peak DHE pixels from S6 using a threshold level of 85%. (B) Location of ECFP-Mem pixels using the same threshold. (C) The nearest neighbor EDF plot (line) and Monte Carlo envelope from 99 simulations for the peak DHE data set and (D) for the peak ECFP-Mem data set.

was not uniform. Also, despite the resulting bright DHE emission in the plasma membrane, DHE also accumulated in various membranes and intracellular organelles, thereby adding to the complexity of isolating long stretches of the plasma membrane. The present investigation developed advanced image analysis techniques not only to provide consistent segmentation of the plasma membrane from intracellular and cytosolic components but also to provide reliable new methods for examining and understanding sterol (DHE) distribution in the plasma membrane of living cells. The statistical behavior of the two types of PM regions (cholesterol-rich, cholesterol-poor) was confirmed by blindfolded statistical tests that arrived at consistent conclusions using different methods.

Visually, each of the probes used herein showed a pattern of pixel grouping within the PM, suggesting clustering. However, a more consistent assessment was needed to determine the statistical significance of the observed distributions. Subsequently, a test of CSR was performed upon PM segments using the nearest neighbor distances of pixels of detected DHE, ECFP-Mem, and $DiOC_{18}(3)$ emission in living L-cell fibroblasts. A main assumption for spatial randomness was that the number of points in this area follows a Poisson distribution and, given the events in the area, the position of these points were an independent random sample from a uniform distribution. In each case, CSR was rejected from one-sided Monte Carlo tests at the 1% level. Furthermore, the fact the largest proportion (~69%) of the nearest neighbor distances of DHE distributions gave the probabilistic assessments on the spatial distribution of the pixels of dehydroergosterol emission indicates that there was an underlying clustered (rather than spatially random) pattern to sterol distribution in the plasma membrane of living cells with cluster patterns of highest sterol emission exhibiting typical lengths of 3 pixels (565 nm). Notwithstanding the statistical properties of these patterns, these data for the first time provided support for the existence of sterol-rich and -poor regions in the plasma membrane of living cells and were achieved without cell perturbation (e.g., cholesterol depletion, treatment with cross-linking reagents or antibodies, etc.). For example, in the isolation of lipid rafts, biochemical methods that use detergents for separating cholesterol-rich lipid rafts

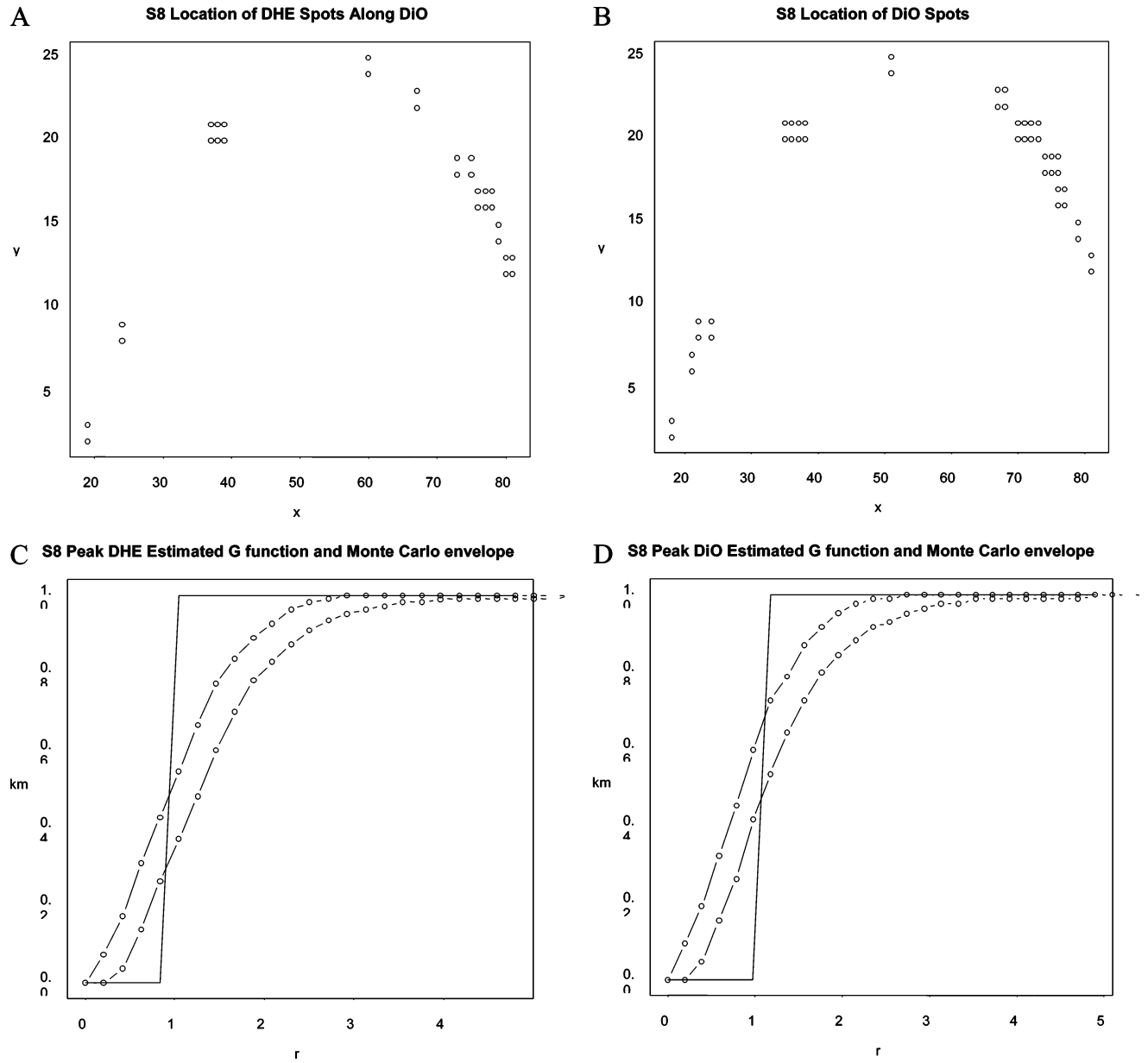

FIGURE 12: Statistical analysis results for S8. (A) Location of peak DHE pixels from S8 using an 85% threshold. (B) Location of peak $DiOC_{18}(3)$ pixels using the same threshold. (C) The nearest neighbor EDF plot (line) and Monte Carlo envelope from 99 simulations for the peak DHE data set and (D) for the peak $DiOC_{18}(3)$ data set.

(i.e., detergent-resistant membranes) yielded ranges of proportions of cholesterol-rich domains from almost none to essentially the entire membrane, depending on the temperature used during the isolation procedure (*8*, *21*). In contrast, another biochemical method that does not use detergents suggested that the cholesterol-rich lipid rafts comprise very little (a few percent) of the plasma membrane (*19*). Through MPLSM acquisition of actual sterol distributions in living cells, the results presented herein established that sterol-rich regions comprise a significant (nearly 30%) part of the extracted plasma membrane section. Consistent with this observation, when the purified plasma membrane isolated from L-cells was resolved into lipid raft/caveolae and nonraft-enriched fractions by affinity chromatography, the lipid rafts/caveolae fraction constituted about 30% of the plasma membrane (*52*).

Although it is known that the cell surface of most cells contains a variety of membrane extrusions, the size range of the DHE-rich domains, i.e., <565 nm, suggested that the DHE-rich domains were not likely to be an artificial result of plasma membrane morphology. For enhancement of emission from randomized sterol domains, a high degree of overlap would be necessary for statistical significance, especially in peak data sets with their narrowed intensity histograms. Largely, plasma membrane folding was not observed in the electron micrographs of mouse fibroblasts (*53*, *54*), and the segments in this analysis were selected away from areas of the "sheetlike" regions of lamellipodia and the very long cylindrical projections of filopodia. On the other hand, these selected regions would contain the smaller cellular projections, microvilli. Electron microscopy of LM fibroblasts revealed that microvilli with widths of approximately 100 nm and lengths on the order of 1000 nm protruded mostly outward (normal to the surface) from much of the plasma membrane surface area (*53*−*55*). This was unlike the situation in other cell types, such as in human

fibroblasts (*56*) and in cells overexpressing certain ezrin/radixin/moesin binding membrane proteins (*55*), where significantly larger microvilli have been observed. In the present analysis, typical cluster lengths were ~565 nm, significantly smaller than the typical length of microvilli in L-cell fibroblasts. If the nearest neighbor distances were *solely* due to enhancement of randomized DHE distributions in folded microvilli, the clustering observed in peak pixels of ECFP-Mem and $DiOC_{18}(3)$ should strongly correlate with the clustering of DHE pixels. There was positive correlation of the ECFP-Mem with DHE but not at the level necessary for all observed DHE clustering to be purely a result of microvilli folding in such a way as to give the appearance of domains. Certainly, the data were consistent with the majority of the clustering due to sterol enrichment in optically resolvable regions rather than the sole enhancement of randomized domains provided by microvilli folded along the excitation plane. This does not preclude the observed clustering from originating from sterol domains within microvilli. Interestingly, microvilli were reported to contain cholesterol-enriched raft domains (*57*), and the regions where DHE correlated well could be indicative of sterol-enriched regions residing within microvilli.

The analysis of $DiOC_{18}(3)$ revealed the largest amount of cluster overlap with DHE and exhibited much higher positive correlation, but notably the peak clustering of DHE also occurred in some areas void of $DiOC_{18}(3)$ clustering and vice versa. The high degree of positive correlation between DHE and the probe, $DiOC_{18}(3)$, could be explained by the fact that $DiOC_{18}(3)$ preferentially locates in ordered phases (*58*) and could represent rafts or raft-like domains. Furthermore, those areas wherein DHE did not colocalize with $DiOC_{18}(3)$ could represent other areas of sterol enrichment of large structures such as coated pits (*59*) or other vesicles involved in the endocytic recycling pathway (*6*, *33*, *34*, *60*−*62*). In fact, the coalesced DHE could represent budding or docking places for sterol transport. However, the high correlation involved with clustering in these two lipids underlined the importance of ordered lipid phases within the plasma membrane.

Membrane domain sizes similar to those reported herein with the fluorescent cholesterol analogue, DHE, were observed in other studies involving various techniques and probes as well as different cell types. A previous imaging study involved fluorescently tagged phospholipids in human coronary artery smooth muscle (HASM) cells (*63*). A saturated phospholipid, DMPE (1,2-dimyristoyl-*sn*-glycero-3-phosphoethanolamine), and a monounsaturated phopholipid, DOPE (1,2-dioleoyl-*sn*-glycero-3-phosphoethanolamine), were tagged with the fluorescent label Cy5, inserted by vesicular exchange with the PM, and imaged by fluorescence microscopy with a 633 nm dye laser and liquid nitrogen-cooled CCD camera (*63*). The sizes of domains exhibiting liquid-ordered phase characteristics ranged between 200 and 2000 nm with a calculated mean of 700 nm and covered approximately 13% of the total plasma membrane area. This investigation also provided analysis of single probe molecule trajectories monitored over time which showed the saturated probe undergoing fast but restricted diffusion in a confined area. The lengths of these confinement regions, evidenced by the dye molecule trajectory, were in the range of 620−700 nm (*63*). In another report, several micron size sterol-rich domains were observed by filipin staining in the plasma membranes of the fission yeast, *Schizosaccharomyces pombe* (*64*). The formation of these domains of ergosterol occurred in the middle or the tips of the cell, which are regions of cell growth and cytokinesis. However, filipin has been shown to disrupt raft/caveolar domains, and filipin staining has not always provided accurate reporting of sterol in the plasma membrane of cells, since proteins underlying the cell surface membrane can affect the filipin staining of sterol (reveiwed in ref *6*).

While spatial localizations of high concentrations of DHE have dimensions larger than those of caveolae, a subclass of lipid rafts (*18*), the resolution of optical microscopy is sufficient to directly visualize clusters of caveolae. Typical caveolae, first seen using electron microscopy as flask-shaped invaginations of the plasma membrane, are in the range of 50−100 nm. The size of the DHE-rich domains obtained by MPLSM (i.e., <650 nm) is in the range of clusters of caveolae, consistent with clustering of the caveolae domains shown by use of protein markers (*57*, *65*). Caveolae are also observable in clustered formations along the plasma membranes of HeLa and MDCK cells as detected by GFP-tagged caveolin protein in both fluorescence and immunogold techniques (*66*). Further investigation involving caveolin-1 and the identification of filamin as a ligand of caveolin-1 also produces evidence of groupings of multiple caveolae in the plasma membranes of NIH/353 fibroblasts and T4.5 trophoblasts (*16*).

Clearly, this investigation supports the evidence of sterol residing in raft and nonraft structures within the PM. The many different subtypes of these PM structures present many challenges in understanding sterol storage, metabolism, and trafficking within cells. Moreover, isolating each individual sterol contribution in PM structures, such as rafts, caveolae, coated pits, endocytic vesicles, and microvilli, is beyond the scope of this paper. Notwithstanding, the techniques developed and reported herein form a strong statistical analysis framework for examining the overall organization of PM sterol at the cellular level.

In summary, the techniques presented herein demonstrated that a fluorescent sterol analogue (DHE), shown to mimic cholesterol in membrane packing and cellular functionality, forms enriched clustered patches within in the plasma membrane with typical sizes near 650 nm. Similar peak clustering of $DiOC_{18}(3)$ took place within many of these sterol-enriched patches indicating not only the involvement of a substantial portion of the DHE in highly ordered domains but probabilistic tendencies for these types of domains to group in ranges that are optically resolvable but yet with a typical maximal size. Two probes that particularly label the PM provided verification of the success of the segmentation technique while statistical spatial point pattern analysis of the real-time images of plasma membrane DHE of L-cell fibroblasts revealed the underlying clustered (rather than random) pattern to sterol distribution in the plasma membrane of living cells. The analyses established that sterol enrichment in living cells occurs within a substantial portion of the plasma membrane (27−40%) with the areas of highest sterol enrichment (4−10%) exhibiting the clustering patterns of lengths <565 nm. These findings have contributed to our understanding of a major unanswered question regarding the uncertainty of the relative proportion of cholesterol-rich

versus cholesterol-poor domains in plasma membranes of living cells by directly probing these domains through the use of a fluorescent sterol, MPLSM, and statistical image analysis.

APPENDIX

(1) Rank-Based Comparison Procedure. For each $i = 1$, 2 window, there were r_i (in our case, $r_i = k^2$) pixels with intensity $[f_{i1}, f_{i2}, ..., f_{ir_i}]$. The combined $N = \sum_{i=1}^{2} r_i$ (in our case, $N = 2k^2$) pixels from the two windows and their intensities (f_{ij}) at each pixel were ranked from smallest to largest. R_{ij} was then designated as the rank of f_{ij} in the combined sample. The total and mean rank was computed as

$$R_i = \sum_{j=1}^{r_i} R_{ij} \qquad \bar{R}_i = \frac{R_i}{r_i}$$

Miller's rank statistic was calculated; that is, the density distributions of pixels in two windows were considered to be different if

$$|\bar{R}_i - \bar{R}_j| \geq q(\alpha,t,\infty)\sqrt{\frac{2(N+1)}{12}}$$

where q was the value for the studentized range (*67*). Of course, different segmentation results were obtained when different threshold values were used.

(2) Smoothed Geometric Trajectory of the PM Zone Using Moments Functions. Moments methods have been widely used in image processing applications for shape analysis. Geometric moments of different orders capture different spatial characteristics of the image's intensity distribution (*68*, *69*), where high-order moments were more sensitive to noise.

The geometric moments of an image were defined as

$$m_{pq} = \int_R\int x^p y^q (x,y)\, \mathrm{d}x\, \mathrm{d}y \qquad p,q = 0, 1, 2, 3, ... \quad (1)$$

where m_{pq} is the $(p + q)$th order moment of the continuous image function $f(x,y)$ over the region R. For digital images the integrals were replaced by summations, and m_{pq} became

$$m_{pq} = \sum_x \sum_y x^p y^q f(x,y) \quad (2)$$

By definition, the zeroth order moment m_{00} represented the total intensity in the region. The first-order moments, m_{10} and m_{01}, provided the intensity information along the x-axis and the y-axis, respectively. The intensity centroid (x_0,y_0) of the region was given by

$$x_0 = m_{10}/m_{00} \qquad y_0 = m_{01}/m_{00} \quad (3)$$

The moments computed with respect to the intensity centroid were called central moments and were defined as

$$\mu_{pq} = \int_R\int (x - x_0)^p (y - y_0)^q f(x,y)\, \mathrm{d}x\, \mathrm{d}y \quad (4)$$

The second-order central moments μ_{20}, μ_{02} gave the variances about the centroid, and the covariance measure was given by μ_{11}.

The PM area under analysis typically had a long, narrow shape that was roughly characterized as a rectangle, centered at the intensity centroid. As such, the PM "band/belt" was modeled into rectangle segments. The width and length of each rectangular segment were respectively denoted by variables a and b and were determined on the basis of the characteristics of each individual data set. The objective was to delineate a smooth PM trajectory, and its perpendicular components, so DHE measurements took place along these two directions. Here, the second-order *geometric moments* function was adopted to create the two reference directions over a PM area, based on the observation that DHE spots on the PM had the largest degree of "lengthening" along a particular direction, i.e., the PM trajectory, and the maximum "widening" along its perpendicular directions (*47*). These two directions were referred to as *principal axes* of the shape under analysis, and they had the largest and smallest variances for the signal samples through the intensity centroid of the shape.

In the experiments presented herein, the value of a ranged from 6 to 7 pixels, and b ranged from 1 to 3 pixels. This represented relatively fine resolution in calculating the trajectory shapes of the PM at this level of analysis. The $a \times b$ window around a selected pixel was called its *PM window*. The second-order moments of a data set are widely used to determine the principal axes. By setting the reference line along the direction that had the maximal lengthening, the probability of losing data was minimized when an enveloped measurement of DHE was taken along the trajectory. To facilitate the actual DHE measurement over the PM, the objective here was to create a smoothed, continuous PM trajectory map.

The intensity centroid of a $w \times w$, $w > a, b$, *smoothing window* of a pixel located at (X,Y) was calculated. On the basis of empirical results, w was set to be 20 pixels. This allowed calculation of the PM window of the intensity centroid. If the central pixel (X,Y) of the smoothing window fell inside the PM window of the intensity centroid, then the pixel's intensity was replaced by the average value of its $n \times n$ neighboring pixels. In this study, n was set to be 5. Otherwise, the value of the pixel (X,Y) was set to be zero. On the basis of the definition of central moments, the following was obtained:

$$a = 4(I_1/m_{00})^{1/2} \qquad b = 4(I_2/m_{00})^{1/2} \quad (5)$$

where

$$I_1 = ((\mu_{20} + \mu_{02}) + [(\mu_{20} - \mu_{02})^2 + 4\mu_{11}{}^2]^{1/2})/2 \quad (6)$$

$$I_2 = ((\mu_{20} + \mu_{02}) - [(\mu_{20} - \mu_{02})^2 + 4\mu_{11}{}^2]^{1/2})/2 \quad (7)$$

The orientation of the rectangle was determined by

$$\theta = {}^1/_2 \tan^{-1}(2\mu_{11}/(\mu_{20} - \mu_{02})) \quad (8)$$

The algorithm for the smoothing PM region was formally described as follows.

Step 1: For any pixel at (X,Y), define its smoothing window $R(X,Y)$ as

$$R(X,Y) = \{(x,y):\ |x - X| \le w/2 \quad \text{and} \quad |y - Y| \le w/2\} \tag{9}$$

Step 2: Find the intensity centroid (x_0,y_0) of $R(X,Y)$ and calculate its second-order moments μ_{20}, μ_{02}, and μ_{11}.

Step 3: Calculate the PM window of the intensity centroid, which is represented by a rectangle, whose size and orientation are evaluated by eqs 5 and 8.

Step 4: If the pixel at (X,Y) is inside the PM window of the intensity centroid, or

$$|(X - x_0)\cos\theta + (Y - y_0)\sin\theta| \le a/2$$

and

$$|(X - x_0)\sin(-\theta) + (Y - y_0)\cos\theta| \le b/2$$

then $f(X,Y) = \text{avg}(R)$; otherwise, $f(X,Y) = 0$.

(3) Monte Carlo Test. In the Monte Carlo test, $s - 1$ random samples u_i, $i = 2, ..., s$, of the same size as the DHE pixels are generated under the null hypothesis, which DHE pixels have a CSR point pattern, and let $u_{(j)}$ denote the jth largest among u_i, $i = 1, ..., s$. Then, under the null hypothesis (*48*)

$$P\{u_1 = u_{(j)}\} = s^{-1} \qquad j = 1, ..., s$$

Rejection of the null hypothesis occurs if u_1 rank kth largest or higher gives an exact, one-sided test of size k/s. For a one-sided test at the conventional 1% level, $s = 100$ is adequate.

The Monte Carlo simulation was used to form a simulation envelope as follows: The EDF points $\hat{G}_i(y)$, $i = 2, 3, ..., s$, were calculated from $s - 1$ independent simulations of n (e.g., $n = 114$ for S1) spots that were independently and uniformly distributed on A. The area A formed from fitting a 95% predict interval over DHE spots. The upper and lower bounds of the simulation were defined as (*48*)

$$U(y) = \max_{i=2,...,s}\{\hat{G}_i(y)\} \qquad L(y) = \min_{i=2,...,s}\{\hat{G}_i(y)\} \tag{10}$$

The maxima and minima of each testing point were set as the upper and lower bounds of the testing point. Each testing point was simulated for a given number s (99 times in this study) of simulation runs, and based on the rank of $\hat{G}_1(y)$ among $s - 1$ $\hat{G}_i(y)$'s, a conclusion was derived (*48*, *50*, *70*).

After the simulations, $\hat{G}_1(y)$ and the Monte Carlo envelopes were plotted against the $G(y)$. If the data set is compatible with CSR, the EDF line should fall inside the envelopes. The data set was called a cluster pattern if the data set line exceeds the upper part of the Monte Carlo envelope and a regular pattern if it was below the lower part of the Monte Carlo envelope (*48*).

REFERENCES

1. Brown, M. S., and Goldstein, J. L. (1986) A receptor-mediated pathway for cholesterol homeostasis, *Science 232*, 34−47.
2. Small, D. M. (1988) Progression and regression of atherosclerotic lesions. Insights from lipid physical chemistry, *Arteriosclerosis 8*, 103−129.
3. Tabas, I. (1997) Free cholesterol-induced cytotoxicity, *Trends Cardiovasc. Med. 7*, 256−263.
4. Sokol, J., Blanchette-Mackie, E. J., Kruth, H. S., Dwyer, N. K., Amende, L. M., Butler, J. D., Robinson, E., Patel, S., Brady, R. O., Comly, M. E., Vanier, M. T., and Pentchev, P. (1988) Type C Niemann-Pick disease: lysosomal accumulation and defective intracellular mobilization of LDL cholesterol, *J. Biol. Chem. 263*, 3411−3417.
5. Fielding, C. J., and Fielding, P. E. (1997) Intracellular cholesterol transport, *J. Lipid Res. 38*, 1503−1521.
6. Schroeder, F., Gallegos, A. M., Atshaves, B. P., Storey, S. M., McIntosh, A., Petrescu, A. D., Huang, H., Starodub, O., Chao, H., Yang, H., Frolov, A., and Kier, A. B. (2001) Recent advances in membrane microdomains: rafts, caveolae, and intracellular cholesterol trafficking, *Exp. Biol. Med. 226*, 873−890.
7. Anderson, R. (1998) The caveolae membrane system, *Annu. Rev. Biochem. 67*, 199−225.
8. Brown, D. A., and London, E. (2000) Structure and function of sphingolipid- and cholesterol-rich membrane rafts, *J. Biol. Chem. 275*, 17221−17224.
9. Hooper, N. M. (1999) Detergent-insoluble glycosphingolipid/cholesterol rich membrane domains, lipid rafts, and caveolae, *Mol. Membr. Biol. 16*, 145−156.
10. Simons, K., and Ikonen, E. (1997) Functional rafts in cell membranes, *Nature 387*, 569−572.
11. Fielding, C. J., and Fielding, P. E. (2000) Cholesterol and caveolae: structural and functional relationships, *Biochim. Biophys. Acta 1529*, 210−222.
12. Samsonov, A. V., Mihalyov, I., and Cohen, F. S. (2001) Characterization of cholesterol-sphingomyelin domains and their dynamics in bilayer membranes, *Biophys. J. 81*, 1486−1500.
13. Ikonen, E., and Parton, R. G. (2000) Caveolins and cellular cholesterol balance, *Traffic 1*, 212−217.
14. Kurzchalia, T. V., and Parton, R. G. (1999) Membrane microdomains and caveolae, *Curr. Opin. Cell Biol. 11*, 424−431.
15. Lundbaek, J. A., Andersen, O. S., Werge, T., and Nielsen, C. (2003) Cholesterol-induced protein sorting: an analysis of energetic feasibility *Biophys. J. 84*, 2080−2089.
16. Stahlhut, M., Sandvig, K., and van Deurs, B. (2000) Caveolae: Uniform Structures with Multiple Functions in Signaling, Cell Growth, and Cancer, *Exp. Cell Res. 261*, 111−118.
17. Pierini, L. M., and Maxfield, F. R. (2001) Commentary flotillas of lipid rafts fore and aft, *Proc. Natl. Acad. Sci. U.S.A. 98*, 9471−9473.
18. Anderson, R. G. W., and Jacobson, K. (2002) A role for lipid shells in targeting proteins to caveolae, rafts, and other lipid domains, *Science 296*, 1821−1825.
19. Smart, E. J., Ying, Y., Mineo, C., and Anderson, R. G. W. (1995) A detergent-free method for purifying caveolae membrane from tissue culture cells, *Proc. Natl. Acad. Sci. U.S.A. 92*, 10404−10408.
20. Schroeder, R., London, E., and Brown, D. (1994) Interactions between saturated acyl chains confer detergent resistance on lipids and glycosylphosphatidylinositol (GPI)-anchored proteins: GPI-anchored proteins in liposomes and cells show similar behavior, *Proc. Natl. Acad. Sci. U.S.A. 91*, 12130−12134.
21. Brown, D. A., and London, E. (1998) Structure and origin of ordered lipid domains in biological membranes, *J. Membr. Biol. 164*, 103−114.
22. Pike, L. J., Han, X., Chung, K.-N., and Gross, R. W. (2002) Lipid rafts are enriched in arachidonic acid and plasmenylethanolamine and their composition is independent of caveolin-1 expression: a quantitative electrospray ionization/mass spectrometric analysis, *Biochemistry 41*, 2075−2088.
23. McIntosh, A., Gallegos, A., Atshaves, B. P., Storey, S., Kannoju, D., and Schroeder, F. (2003) Fluorescence and multiphoton imaging resolve unique structural forms of sterol in membranes of living cells, *J. Biol. Chem. 278*, 6384−6403.
24. Eckert, G. P., Igbavboa, U., Muller, W., and Wood, W. G. (2003) Lipid rafts of purified mouse brain synaptosomes prepared with or without detergent reveal different lipid and protein domains, *Brain Res. 962*, 144−150.
25. London, E., and Brown, D. A. (2000) Insolubility of lipids in Trition X-100: physical origin and relationship to sphingolipid/cholesterol membrane domains (rafts), *Biochim. Biophys. Acta 1508*, 182−195.
26. Hale, J. E., and Schroeder, F. (1982) Asymmetric transbilayer distribution of sterol across plasma membranes determined by fluorescence quenching of dehydroergosterol, *Eur. J. Biochem. 122*, 649−661.
27. Schroeder, F., and Nemecz, G. (1990) in *Advances in Cholesterol Research* (Esfahami, M., and Swaney, J., Eds.) pp 47−87, Telford Press, Caldwell, NJ.

28. Schroeder, F. (1984) Fluorescent sterols: probe molecules of membrane structure and function, *Prog. Lipid Res. 23*, 97−113.
29. Schroeder, F., Jefferson, J. R., Kier, A. B., Knittell, J., Scallen, T. J., Wood, W. G., and Hapala, I. (1991) Membrane cholesterol dynamics: cholesterol domains and kinetic pools, *Proc. Soc. Exp. Biol. Med. 196*, 235−252.
30. Gimpl, G., Burger, K., and Fahrenholz, F. (1997) Cholesterol as modulator of receptor function, *Biochemistry 36*, 10959−10974.
31. Schroeder, F., Frolov, A., Schoer, J., Gallegos, A., Atshaves, B. P., Stolowich, N. J., Scott, A. I., and Kier, A. B. (1998) in *Intracellular Cholesterol Trafficking* (Chang, T. Y., and Freeman, D. A., Eds.) pp 213−234, Kluwer Academic Publishers, Boston, MA.
32. Frolov, A., Petrescu, A., Atshaves, B. P., So, P. T. C., Gratton, E., Serrero, G., and Schroeder, F. (2000) High-density lipoprotein mediated cholesterol uptake and targeting to lipid droplets in intact L-cell fibroblasts, *J. Biol. Chem. 275*, 12769−12780.
33. Mukherjee, S., Zha, X., Tabas, I., and Maxfield, F. R. (1998) Cholesterol distribution in living cells: fluorescence imaging using dehydroergosterol as a fluorescent cholesterol analog, *Biophys. J. 75*, 1915−1925.
34. Wustner, D., Herrmann, A., Hao, M., and Maxfield, F. R. (2002) Rapid nonvesicular transport of sterol between the plasma membrane domains of polarized hepatic cells, *J. Biol. Chem. 277*, 30325−30336.
35. Williams, R. M., Zipfel, W. R., and Webb, W. W. (2001) Multiphoton microscopy in biological research, *Curr. Opin. Chem. Biol. 5*, 603−608.
36. Xu, C., Zipfel, W. R., Shear, J. B., Williams, R. M., and Webb, W. W. (1996) Multiphoton fluorescence excitation: new spectral windows for biological nonlinear spectroscopy, *Proc. Natl. Acad. Sci. U.S.A. 93*, 10763−10768.
37. Huang, H., Starodub, O., McIntosh, A., Kier, A. B., and Schroeder, F. (2002) Liver fatty acid binding protein targets fatty acids to the nucleus: real-time confocal and multiphoton fluorescence imaging in living cells, *J. Biol. Chem. 277*, 29139−29151.
38. Rocheleau, J. V., Wiseman, P. W., and Petersen, N. O. (2003) Isolation of bright aggregate fluctuations in a multipopulation image correlation spectroscopy system using intensity subtraction, *Biophys. J. 84*, 4011−4022.
39. Petersen, N. O., Hoddelius, P. L., Wiseman, P. W., Seger, O., and Magnusson, K. E. (1993) Quantitation of membrane receptor distributions by image correlation spectroscopy: concept and application, *Biophys. J. 65*, 1135−1146.
40. Elson, E. L., and Webb, W. W. (1975) Concentration correlation spectroscopy: a new biophysical probe based on occupation number fluctuations, *Annu. Rev. Biophys. Bioeng. 4*, 311−334.
41. Magde, D., Elson, E. L., and Webb, W. W. (1974) Fluorescence correlation spectroscopy. II. An experimental realization, *Biopolymers 13*, 29−61.
42. McCaughan, L., and Krimm, S. (1980) X-ray and neutron scattering density profiles of the intact human red blood cell membrane, *Science 207*, 1481−1483.
43. Kaplan, M. R., and Simoni, R. D. (1985) Transport of cholesterol from the endoplasmic reticulum to the plasma membrane, *J. Cell Biol. 101*, 446−453.
44. Fischer, R. T., Stephenson, F. A., Shafiee, A., and Schroeder, F. (1985) Structure and dynamic properties of dehydroergosterol, Δ5,7,9(11),22-ergostatetraen-3β-ol, *J. Biol. Phys. 13*, 13−24.
45. Ruthazer, E. S., and Cline, H. T. (2002) Multiphoton imaging of neurons in living tissue: acquisition and analysis of time-lapse morphological data, *Real-Time Imaging 8*, 175−188.
46. Hollander, M., and Wolfe, D. A. (1999) *Nonparametric Statistical Methods*, John Wiley & Sons, New York.
47. Mukundan, R., and Ramakrishnan, K. R. (1998) *Moment Function in Image Analysis: Theory and Applications*, World Scientific, River Edge, NJ.
48. Diggle, P. J. (1983) *Statistical Analysis of Spatial Point Patterns*, Academic Press, New York.
49. Baddeley, A. J., and Gill, R. D. (1997) Kaplan-Meier estimators of interpoint distance distributions for spatial point processes, *Ann. Stat. 25*, 263−292.
50. Bernard, G. A. (1963) Contribution to the discussion of Professor Bartlett's paper, *J. R. Stat. Soc. B25*, 294.
51. *R project for statistical computing*, http://www.r-project.org/index.html.
52. Atshaves, B. P., Gallegos, A., McIntosh, A. L., Kier, A. B., and Schroeder, F. (2003) Sterol carrier protein-2 selectively alters lipid composition and cholesterol dynamics of caveolae/lipid raft vs non-raft domains in L-cell fibroblast plasma membranes, *Biochemistry 42*, 14583−14598.
53. Schroeder, F., Fontaine, R. N., and Kinden, D. A. (1982) LM fibroblast plasma membrane subfractionation by affinity chromatography on ConA-sepharose, *Biochim. Biophys. Acta 690*, 231−242.
54. Schroeder, F., and Kinden, D. A. (1983) Measurement of phagocytosis using fluorescent latex beads, *J. Biochem. Biophys. Methods 8*, 15−27.
55. Yonemura, S., Tsukita, S., and Tsukita, S. (1999) Direct involvement of ezrin/radixin/moesin (ERM)-binding membrane proteins in the organization of microvilli in collaboration with activated ERM proteins, *J. Cell Biol. 145*, 1497−1509.
56. Puri, V., Watanabe, R., Singh, R. D., Dominguez, M., Brown, J. C., Wheatley, C. L., Marks, D. L., and Pagano, R. E. (2001) Clathrin-dependent and -independent internalization of plasma membrane sphingolipids initiates two Golgi targeting pathways, *J. Cell Biol. 154*, 535−547.
57. Roper, K., Corbeil, D., and Huttner, W. B. (2000) Retention of prominin in microvilli reveals distinct cholesterol-based lipid microdomains in the apical plasma membrane, *Nat. Cell Biol. 2*, 582−592.
58. Spink, C. H., Yeager, M., and Feigenson, G. W. (1990) Partitioning behavior of indocarbocyanine probes between coexisting gel and fluid phases in model membranes, *Biochim. Biophys. Acta 1023*, 25−33.
59. Pearse, B. M. F. (1976) Clathrin: a unique protein associated with intracellular transfer of membrane by coated vesicles, *Proc. Natl. Acad. Sci. U.S.A. 73*, 1255−1259.
60. Mukherjee, S., Ghosh, R. N., and Maxfield, F. R. (1997) Endocytosis, *Physiol. Rev. 77*, 759−803.
61. Hao, M., and Maxfield, F. R. (2000) Characterization of rapid membrane internalization and recycling, *J. Biol. Chem. 275*, 15279−15286.
62. Hao, M., Lin, S. X., Karylowski, O. J., Wustner, D., McGraw, T. E., and Maxfield, F. R. (2002) Vesicular and non-vesicular sterol transport in living cells: the endoytic recycling compartment is a major sterol storage organelle, *J. Biol. Chem. 277*, 609−617.
63. Schutz, G. J., Kada, G., Pastushenko, V. Ph., and Schindler, H. (2000) Properties of lipid microdomains in a muscle cell membrane visualized by single molecule microscopy, *EMBO J. 19*, 892−901.
64. Wachtler, V., Rajagopalan, S., and Balasubramanian, M. K. (2003) Sterol-rich plasma membrane domains in the fission yeast *Schizosaccharomyces pombe*, *J. Cell Sci. 116*, 867−874.
65. Prior, I. A., Muncke, C., Parton, R. G., and Hancock, J. F. (2003) Direct visualization of Ras proteins in spatially distinct surface microdomains, *J. Cell Biol. 160*, 165−170.
66. Thomsen, P., Roepstorff, K., Stahlhut, M., and van Deurs, B. (2002) Caveolae are highly immobile plasma membrane microdomains, which are not involved in constitutive endocytic trafficking, *Mol. Biol. Cell 13*, 238−250.
67. Kuehl, R. O. (2000) *Design of Experiments, Statistical Principles of Research Design and Analysis*, Duxbury/Thomson Learning, Pacific Grove, CA.
68. Hu, M. K. (1961) Pattern recognition by moment invariants, *Proc. Inst. Radio Eng. 49*, 1428.
69. Sluzek, A. (1995) Identification and inspection of 2-D objects using new moment-based shape descriptors, *Pattern Recognit. Lett. 16*, 687−697.
70. Gentle, J. E. (2002) *Elements of Computational Statistics*, Springer-Verlag, New York.

BI048172M